EXPERIMENTAL AND DENSITY FUNCTIONAL THEORY STUDY ON GAS SENSING

PROPERTIES OF ZINC OXIDE/GRAPHENE NANOCOMPOSITE

By

MR. Worachote PHOTARAM

A Thesis Submitted in Partial Fulfillment of the Requirements

for Master of Science (PHYSICS)

Department of PHYSICS

Graduate School, Silpakorn University

Academic Year 2020

การศึกษาสมบัติการตรวจจับแก๊สของวัสดุผสมระดับนาโนซิงก์ออกไซด์/กราฟีนโดย
วิธีการทดลองและวิธีการคำนวณด้วยทฤษฎีฟังก์ชันนอลความหนาแน่น

โดย
นายวรโชติ โพธาราม

วิทยานิพนธ์นี้เป็นส่วนหนึ่งของการศึกษาตามหลักสูตรวิทยาศาสตรมหาบัณฑิต
สาขาวิชาฟิสิกส์ แผน ก แบบ ก 2 ระดับปริญญามหาบัณฑิต
ภาควิชาฟิสิกส์
บัณฑิตวิทยาลัย มหาวิทยาลัยศิลปากร
ปีการศึกษา 2563

EXPERIMENTAL AND DENSITY FUNCTIONAL THEORY STUDY ON GAS

SENSING PROPERTIES OF ZINC OXIDE/GRAPHENE NANOCOMPOSITE

By

MR. Worachote PHOTARAM

A Thesis Submitted in Partial Fulfillment of the Requirements

for Master of Science (PHYSICS)

Department of PHYSICS

Graduate School, Silpakorn University

Academic Year 2020

Title	EXPERIMENTAL AND DENSITY FUNCTIONAL THEORY STUDY ON GAS SENSING PROPERTIES OF ZINC OXIDE/GRAPHENE NANOCOMPOSITE
By	Worachote PHOTARAM
Field of Study	(PHYSICS)
Advisor	Assistant Professor Montri Aiempanakit , Ph.D.

Graduate School Silpakorn University in Partial Fulfillment of the Requirements for the Master of Science

.... Dean of graduate school

(Associate Professor Jurairat Nunthanid, Ph.D.)

Approved by

.... Chair person

(Assistant Professor Itsara Masiri , Ph.D.)

.... Advisor

(Assistant Professor Montri Aiempanakit , Ph.D.)

.... Co advisor

(Assistant Professor Chawarat Siriwong , Ph.D.)

.... External Examiner

(Associate Professor Manus Seadan , Ph.D.)
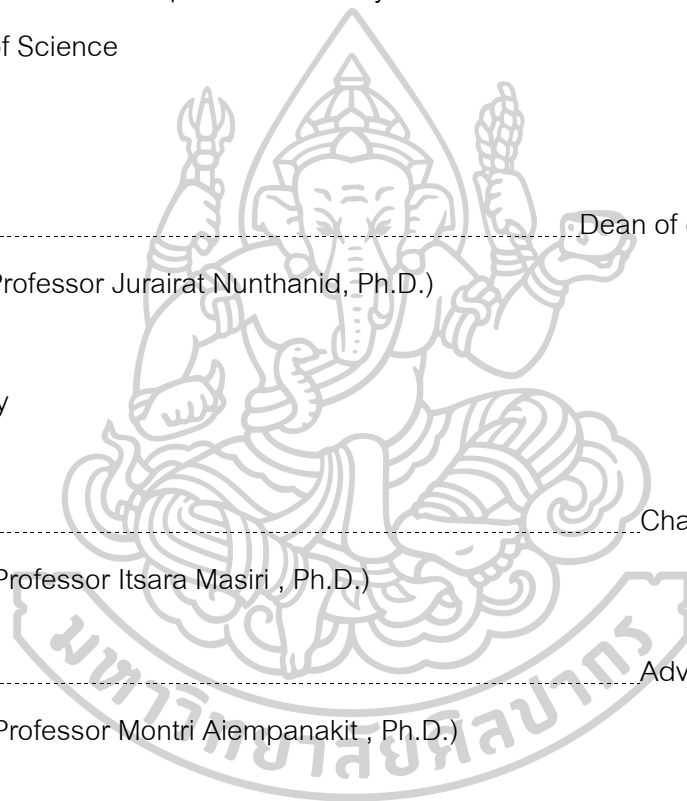
61306201 : Major (PHYSICS)

Keyword : gas sensors, hybrid, nanocomposite, zinc-oxide, graphene, DFT

MR. WORACHOTE PHOTARAM : EXPERIMENTAL AND DENSITY FUNCTIONAL THEORY STUDY ON GAS SENSING PROPERTIES OF ZINC OXIDE/GRAPHENE NANOCOMPOSITE THESIS ADVISOR : ASSISTANT PROFESSOR MONTRI AIEMPANAKIT, Ph.D.

Gas sensors are essential in a variety of applications, and they have been largely developed for detecting exhaust gases and air pollution. However, despite the progress that has been made, a number of challenges remain in terms of achieving the sensing materials with high sensitivity, selectivity, and fast response. This research combines theoretical and experimental analyses to model and fabricate a hybrid ZnO/graphene nanocomposite that can be further modified for the enhanced effectiveness than the individual materials. Theoretically, density functional theory (DFT) was employed to investigate the effects of different hybrid nanocomposites on gas adsorption and electronic properties, when exposed to various gases. The hybrid structures were modeled, including the ZnO/graphene layers (ZnO is the top layer), the graphene/ZnO layer, and the ZnO cluster on the graphene monolayer. The calculations indicate that ZnO cluster/graphene could exhibit relatively strong gas adsorption with the adsorption energy of -0.37 eV when exposed to N_2O gas. Based on the computational part, the candidate matrix was synthesized by varying the graphene contents from 1-10 %W/W. As a result, the graphene content of 5% w/w leads to a reasonably high gas sensitivity of 54.30 upon the 2000 ppm of ethanol gas exposure. This work could make a prominent contribution to the design and fabrication of the gas sensing device with significantly enhanced capabilities.

ACKNOWLEDGEMENTS

TABLE OF CONTENTS

List of tables

List of figures

Chapter 1

Introduction

1.1 Research background and motivation

From the past to the present, air pollution is still a significant problem worldwide and likely to increase continuously along with the national developments. The pollution problems may be caused by numerous reasons. For example, industrial plants release large amounts of gas, gas leaking from machinery, and gas emissions from vehicles. These problems affect human health, especially all industrial workers exposed to harmful gases. To control machines in all factories producing toxic gases, e.g., carbon monoxide (CO), sulfur dioxide (SO_2), and hydrogen sulfide (H_2S), gas sensors are employed to detect leaked gas. There were various standard methods used for gas detection but quite complicated in the measurement process due to the need for a professional technique, and the device is quite large [1]. Over the years, the inventions and developments of gas sensors made them smaller and easy to use. Hence, several types of gas sensors, such as catalytic sensor, infrared sensor, electrochemical sensor, and solid-state sensor (Metal Oxide Semiconductor, MOS), etc., have been investigated [2]. The properties used to select gas sensor types are function, accuracy, lifetime, and cost of production.

At present, metal oxide semiconductors (MOS) gas sensors consisting of n-type or p-type semiconductors are widely used to detect gases at low concentrations [3]. Metal oxide semiconductor sensors respond to the detected gases due to the sensor's resistance changing with the amount of gas concentration. Besides, the MOS gas sensors also have the advantages of low production cost, fast response/recovery time, high sensitivity, ease to use, small in size, long lifetime. They can be used in high-temperature and high-pressure conditions [4]. However, further development of this type of gas sensor is required to make gas sensors capable of detecting low concentration

gases with greater sensitivity, faster response and recovery times, and lower operating temperatures. As a promising candidate for gas detecting, zinc oxide (ZnO) shows its significant potential in applying gas sensors due to its good electrical, structural, and environmentally friendly properties and high response to various reducing and oxidizing gases. Besides the wide bandgap (3.37 eV), the vital factor in attaining high gas sensing response in the ZnO structure system is the rapid recombination of charge carriers. Over the years, composites such as semiconductor-noble metal composites, semiconductor-semiconductor composites, semiconductor-carbon materials composites, and others have proven to be an effective way to increase the performance of ZnO gas sensors. In the last few years, graphene thrives in composite materials according to its conductivity, wide surface area, adsorption capacity, and superior electron mobility, supporting gas sensitivity performances. Consequently, it is thought that a hybrid of flexible and electrically conductive graphene embedded with nanostructured ZnO can effectively combine the advantages of nanosized ZnO and graphene to produce better gas sensors.

This study examines the microscopic properties of ZnO/graphene nanocomposite and understands the mechanism of gas adsorption by using a first-principles calculation based on density functional theory (DFT). The results obtained from the model are binding strength, charge transfer, and other sensing properties of the graphene and ZnO surface, which could be used to design better gas sensing devices. According to the ZnO/graphene substrate from the model, we experimentally investigate gas detection properties of metal oxide semiconductor gas sensor made from ZnO/graphene nanocomposite by using hydrogen (H_2), methane (CH_4), nitrous oxide (N_2O), ammonia (NH_3), acetone ($(CH_3)_2CO$), and ethanol (C_2H_5OH) as detected gases. It is expected that graphene will increase the efficiency of the sensor in response to the detected gases.

1.2 Objectives

1. Using the simulation approach to calculate binding strength, charge transfer, and other sensing properties to find the substrate candidate based on ZnO/graphene nanocomposite suitable for use as a sensing material.

2. To fabricate gas sensors using zinc oxide film and graphene-mixed zinc oxide film as a sensing material.

3. To study the gas selectivity and sensitivity of the fabricated sensing materials towards H_2, CH_4, N_2O, NH_3, $(CH_3)_2CO$, and C_2H_5OH gases.

1.3 Scope of the study

This research combines the theoretical and experimental studies to examine the gas adsorption mechanism and capacity of ZnO/graphene nanocomposite. The scope of the theoretical investigation is as follows:

1. Study of ZnO/graphene nanocomposite substrates including pristine ZnO, pristine graphene, graphene/ZnO, ZnO/graphene, and graphene/ZnO nanocluster surfaces.

2. Study the gas adsorption mechanism of the H_2, CH_4, and N_2O gases on the substrates using DFT

3. Determine the nanocomposite structure indicating the high gas sensitivity and selectivity

The computational results could guide experimental efforts by identifying the candidate material. Followingly, the experiment part covers:

1. Fabricate ZnO and graphene/ZnO gas sensors using spin coating according to the suggested structure from the theoretical study.

2. Study the variables that affect the gas response properties of the sensors exposed to H_2, CH_4, N_2O, NH_3, $(CH_3)_2CO$, and C_2H_5OH, such as the operating temperature, the concentration of graphene additives, and the concentration of gas molecules.

3. Study the properties of gas sensors as follows: sensitivity (S), response time (T_{res}), dynamic range, and operating temperature.

Chapter 2

Literature review

2.1 Relevant principles and theories of gas sensing mechanisms

Standard metal oxide semiconductor-based gas sensing material will change the electric signal when it exposes to target gas. The process of gas sensing has 2 categories (Fig. 1). The first category describes the microscopic viewpoint such as electron depletion layer theory, hole accumulation layer theory, etc. The second is comparatively macroscopic, and its attention is specifically on material-gas relationships. Such theories allow for a clearer understanding of the mechanism of gas sensing reactions based on real physical phenomena through modern material analysis techniques.
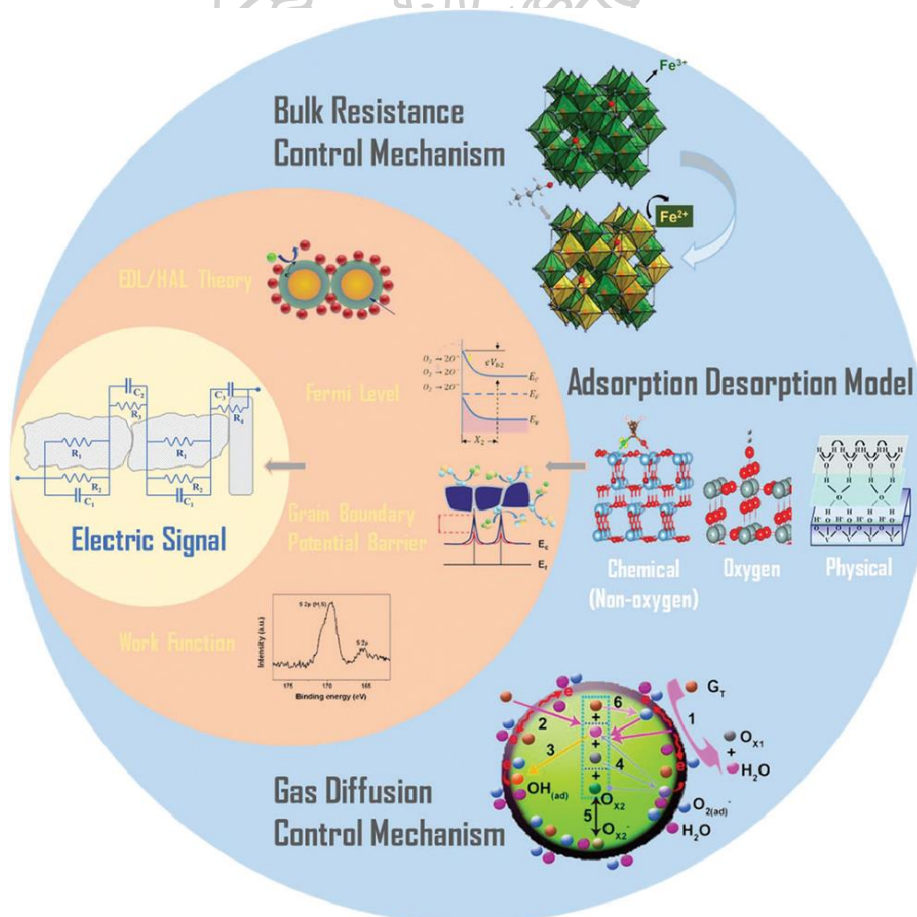
Figure 1 Macroscopic and microscopic gas sensing phenomenal of MOS [5].

2.1.1 Adsorption/desorption models

Scientists have known since the early 20th century that the resistance and work function of a metal oxide semiconductor shift as it exposes to gases like oxygen and carbon monoxide. In reality, the fundamental of recent gas sensing mechanism is the adsorption/desorption model. This model describes the conductance changing cause by the changing of the charge carrier.

1. Oxygen adsorption models

As the most general gas sensing system, the oxygen adsorption model is seen as being appropriate for virtually all metal oxide semiconductor gas sensor, and electron depletion layer and hole accumulation layer models are expansions of the oxygen adsorption models. As a metal oxide semiconductor is applied to the air, oxygen molecules are adsorbed on the surface of the material.

In general, an important mechanism for gas detection of fabricated sensors is the vary in the oxygen species density of the surface of the metal oxide film (such as O^{2-} and O^-). The change is related to two chemical reactions, the first reaction is the reaction between the metal oxide and oxygen molecules. When the sensor is atmospheric conditions. And the second reaction is the interaction of the detected gas and the oxygen species that has been adsorbed. By the model of the gas detection mechanism is shown in Fig. 2.

Mechanism of oxygen species on the metal oxide film surface is caused by the sensor being under heated conditions and under an atmosphere surrounded by oxygen gas. From these conditions, the process of oxygen adsorption occurs. Oxygen is interacted with the film's surface by pulling electrons from the conduction band of MOS. This mechanism causes Schottky potential barriers to occur in the boundary between the grain. Zinc oxide and tin dioxide are examples of n-type metal oxide semiconductors. Electrons that are pulled from the conduction band will increase the thickness of depletion layer in each grain because the density of the carrier charges (electrons) on the surface of thin film are decreased. Which results in the potential barrier at the boundary increased. From the aforementioned process, the sensor made of n-type semiconductor has increased resistance when the sensor is under an atmosphere

surrounded by oxygen gas. But the resistance of the sensor will decrease in p-type semiconductors because the majority of carriers are holes. When electrons are removed from the conduction band due to increased oxygen, the resistance of sensor decreases. The type of oxygen species depends on the temperature, i.e., if the temperature is lower than 150 $^{\circ}$C it is O_2^-, the temperature between 150-400 $^{\circ}$C it is O^-, and at temperature above 400 $^{\circ}$C it is O^{2-}.
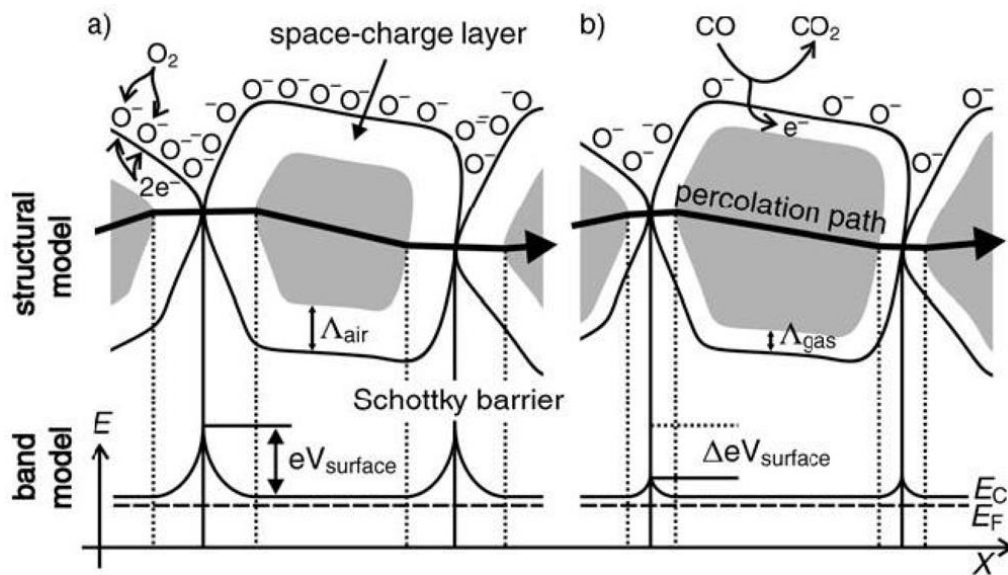
Figure 2 Structure and energy band model of the electrical conductivity mechanism of the metal oxide semiconductor gas sensor (n-type) (a) In the absence of reducing gas entering the reaction (b) In the case of reducing gas expose to the surface [6].

The reaction between the molecules of oxygen and the metal oxide film surface is shown in the equations 1-4. [7]

$$O_{2(g)} \Leftrightarrow O_{2(ads)} \tag{1}$$

$$O_{2(ads)} + e^- \Leftrightarrow O_{2(ads)}^- \tag{2}$$

$$O_{2(ads)}^- + e^- \Leftrightarrow 2O_{(ads)}^- \tag{3}$$

$$2O_{(ads)}^- + e^- \Leftrightarrow O_{(ads)}^{2-} \tag{4}$$

Gas measurements can be divided into 2 groups, the first group is reducing gas and the second group is oxidizing gas. In the gas adsorption process, if it is a reducing gas when the target gas exposes to oxygen species or oxygen ions on the surface of the sensor film, the products of this reaction are a new gas and electron, which the electron return to the conduction band of the metal oxide semiconductor. But if it is an oxidizing gas, the gas reacts with oxygen ions then pulls the electrons out of the conduction band of the sensor surface during the reaction.

1. Reducing gas such as carbon monoxide (CO), hydrogen (H_2), sulfur dioxide (SO_2), ammonia (NH_3), ethanol (C_2H_5OH) and hydrogen sulphide (H_2S), etc. The reaction between oxygen species on surface of the sensor and reducing gas can be expressed as in equation 5-15 [8].

$$2CO + O_2^- \rightarrow 2CO_2 + e^- \tag{5}$$

$$CO + O^- \rightarrow CO_2 + e^- \tag{6}$$

$$H_2 + \frac{1}{2}O_{2(ad)}^- \rightarrow H_2O + e^- \tag{7}$$

$$H_{2(g)} \Leftrightarrow H_{2(ad)} \tag{8}$$

$$H_{2(ad)} \rightarrow 2H^+ + 2e^- \tag{9}$$

$$SO_2 + O_{(s)}^{2-} \rightarrow SO_{3(g)} + 2e^- \tag{10}$$

$$2NH_3 + 3O_{(ads)}^- \rightarrow N_2 + 3H_2O + 3e^- \tag{11}$$

$$C_2H_5OH_{(gas)} + O^- \Leftrightarrow CH_3CHO + H_2O + e^- \tag{12}$$

$$H_2S_{(ads)} + 3O_{(s)}^{2-} \rightarrow SO_{2(g)} + H_2O + 6e^- \tag{13}$$

$$2H_2S_{(ads)} + 3O_{2(s)}^- \rightarrow 2SO_{2(g)} + 2H_2O + 3e^- \tag{14}$$

$$H_2S_{(ads)} + 3O_{(s)}^- \rightarrow SO_{2(g)} + 2H_2O + 3e^- \tag{15}$$
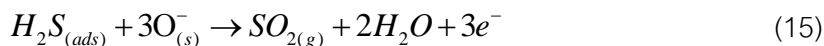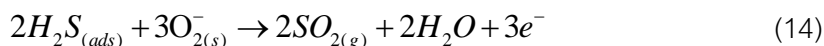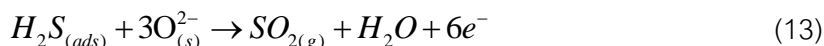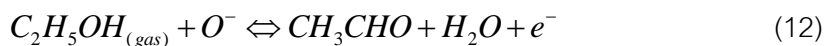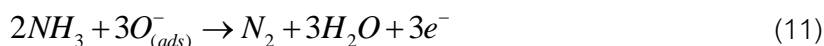
2. Oxidizing gas such as nitrogen dioxide (NO_2) and oxygen (O_2) etc. The reaction between O species over the sensor's surface and oxidizing gas can be expressed as in equation 16-18 [9].

$$NO_{2(gas)} + e^- \rightarrow NO_{2(ads)} \tag{16}$$

$$NO_{2(gas)} + O^-_{2(ads)} + 2e^- \rightarrow NO^-_{2(ads)} + 2O^-_{(ads)} \tag{17}$$

$$NO_{2(gas)} + O^-_{(ads)} \rightarrow NO^+_{(ads)} + 2O^-_{(ads)} \tag{18}$$
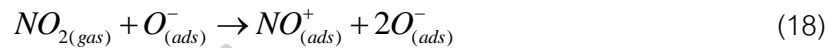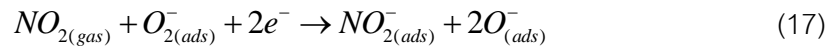
Changes in resistance of metal oxide semiconductor sensors when exposed to gas of each type as shown in Table 1.

Table 1 Resistance of semiconductor sensors that change when exposed to each type of gas

Types of semiconductors	Reducing gas	Oxidizing gas
n-type	Decrease	Increase
p-type	Increase	Decrease

Sensitivity of n-type and p-type metal oxide semiconductor sensors to oxidizing gas are in accordance with the equation (19) and (20) respectively.

$$S^N_{ox} = \frac{R_{og}}{R_a}, \tag{19}$$

$$S^P_{ox} = \frac{R_a}{R_{og}}, \tag{20}$$

where R_{og} is the sensor resistance that can be measured when the sensor expose to oxidizing gas and R_a is the sensor resistance that can be measured when the sensor is in a dry air.

For Sensitivity of n-type and p-type metal oxide semiconductor sensors to reducing gas are in accordance with the equation (21) and (22) respectively.

$$S_{rd}^N = \frac{R_a}{R_{rg}} \,, \tag{21}$$

$$S_{rd}^P = \frac{R_{rg}}{R_a} \,, \tag{22}$$

where R_{rg} is the sensor resistance that can be measured when the sensor expose to reducing gas and R_a is the sensor resistance that can be measured when the sensor is in a dry air.

Examples of changes in the resistance of sensors fabricated from n-type semiconductor when a reducing gas enters the reaction, as shown in Fig. 3.
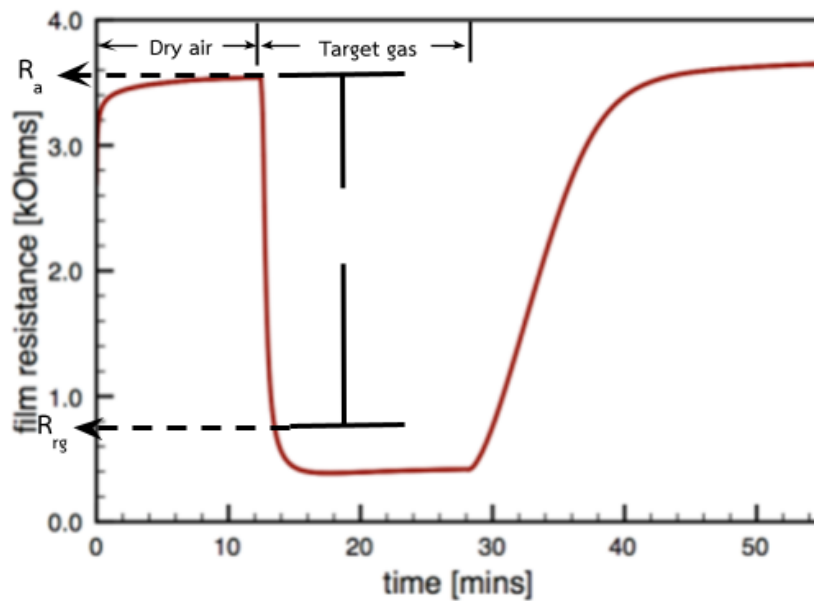
Figure 3 Resistance values of N-type semiconductor sensors when sensor expose to dry air (R_a) and reducing gas (R_{rg}) [10].

2. Chemical adsorption/desorption

When gas exposed directly to crystal grains, causing a transition in electronic impulse, according to the model. Most of the current reports describe the MOS-based sensor gas sensing mechanism but clearly use the concept of direct oxygen adsorption.

Nevertheless, in fact, such an analysis is incomplete in many cases. Many materials, when exposed to a particular gas, inevitably undergo chemical adsorption/desorption and this effect often affects the material's gas sensitivity.

To deeper understand the effect of chemical absorption and desorption of the material's gas sensing capability in interference-free environments, appropriate measurements to a vacuum setting are important [11]. Hence, the chemical absorption and desorption process is a frequently ignored gas response process. In practical research, a thorough examination of the gas sensing method is also needed.

3. Physical adsorption/desorption

The adsorption of gas molecules onto MOS crystals by Coulomb forces, H-bonding, etc. without chemical modification is known as physisorption. The physisorption is a typical physical principle in gas response processes, but it is seldom employed to describe the gas response mechanism. The most popular type of metal oxide semiconductor-based gas sensor is a humidity sensor, which uses physisorption and desorption as the principal gas response process.

Experimental results have shown, using Fe_2O_3 as a humidity sensor as an illustration, it was discovered that Fe_2O_3 nanoparticles have a passive detection capability in low moisture environments. Fig. 4(b) shows that the sensing process could be divided through 2 steps: (1) Chemisorption: molecules of water come into association with the sample surface and separate to create OH^-, which leads to the formation of a hydroxyl film. This mechanism happens at extremely low humidity and with increasing humidity, it does not change any further. (2) Physical adsorption: molecules of water are physiosorbed to the hydroxy surface by H-bonding to create the primary H_2O surface at a high moisture level in the atmosphere. Thereafter, secondary molecules of water are directly interacted over the existing H_2O surface, creating a fresh H_2O surface. This sequence can rise the layers number of H_2O. In each continuous H_2O layer (Fig. 4(c)) proton hopping occurs between adjacent H_2O molecules, cause the creation of persistent electrolyte and dipoles surfaces. Such layers are eventually formed cause the change in impedance and material's conductivity.
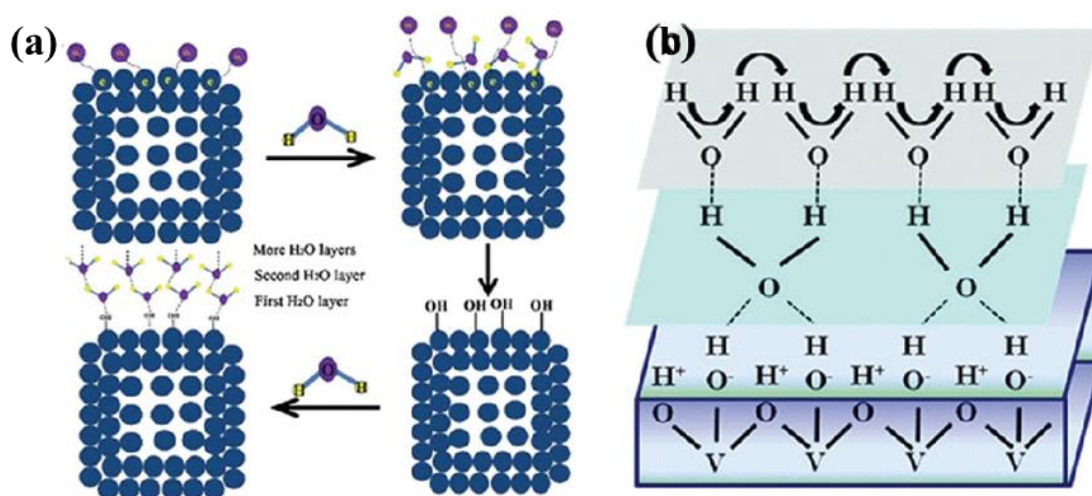
Figure 4 (a) Graphical representation of the humidity response process at various steps [12]; (b) Graphical representation of electron jumping among neighboring molecules of water [13].

2.1.2 Bulk resistance control mechanism

A phase transition of the material that used for gas detection can induce the shift in conductance in certain metal oxide semiconductor. The system, on the other hand, is fairly limited in range, and it can only be used to examine materials including π-Fe_2O_3 and ABO_3 metal oxide semiconductor nanocomposite for gas sensing process.

2.1.3 Gas diffusion control mechanism

The gas sensing process involves two elements, materials, and gases. This part focuses on the gas diffusion mechanism, and the material's morphology is the most important factor influencing that process.

Although this mechanism requires further work in terms of computational study of numerous factors, this commonly employed to determine the influence of metal oxide semiconductor material morphology on its gas response mechanism. This effect can be said to be an important part of the process for the sensing of gas.

2.2 Efforts to enhance gas detection mechanism

The question should be discussed from the viewpoint of the gas sensing mechanism in order to identify the best approach to enhancing the sensor performance of metal oxide semiconductor gas sensors. A detailed analysis of the various mechanisms mentioned above reveals several possible paths. Based on the current adsorption/desorption theory analysis, we will improve MOS sensing performance by enhancing gas binding sites, creating more electron transfer, and increasing active sites to catalyze the response progression.

2.2.1 Introduced high-energy particle facets

Since various aspects of crystals provide specific physical properties, including electrical properties and layer imperfections, gas detection varies significantly. Experiments and first-principle calculations verified this relationship.

Overall, increased gas detection is primarily because of larger hanging bond densities and electron-deficient oxygen synchronization. Using Zinc oxide as such an illustration, the examination of each crystal plane's atomic structure diagram and the calculation of each crystal plane's dangling bond density (Fig. 5) demonstrate that the intensity of the (0 0 0 1) plane is higher. Whenever the gas response mechanism starts, the hanging bonds formed by Zn^{2+} have electron-deficient oxygen interaction over detected layer, and then that spots could be better sites for gas detection.
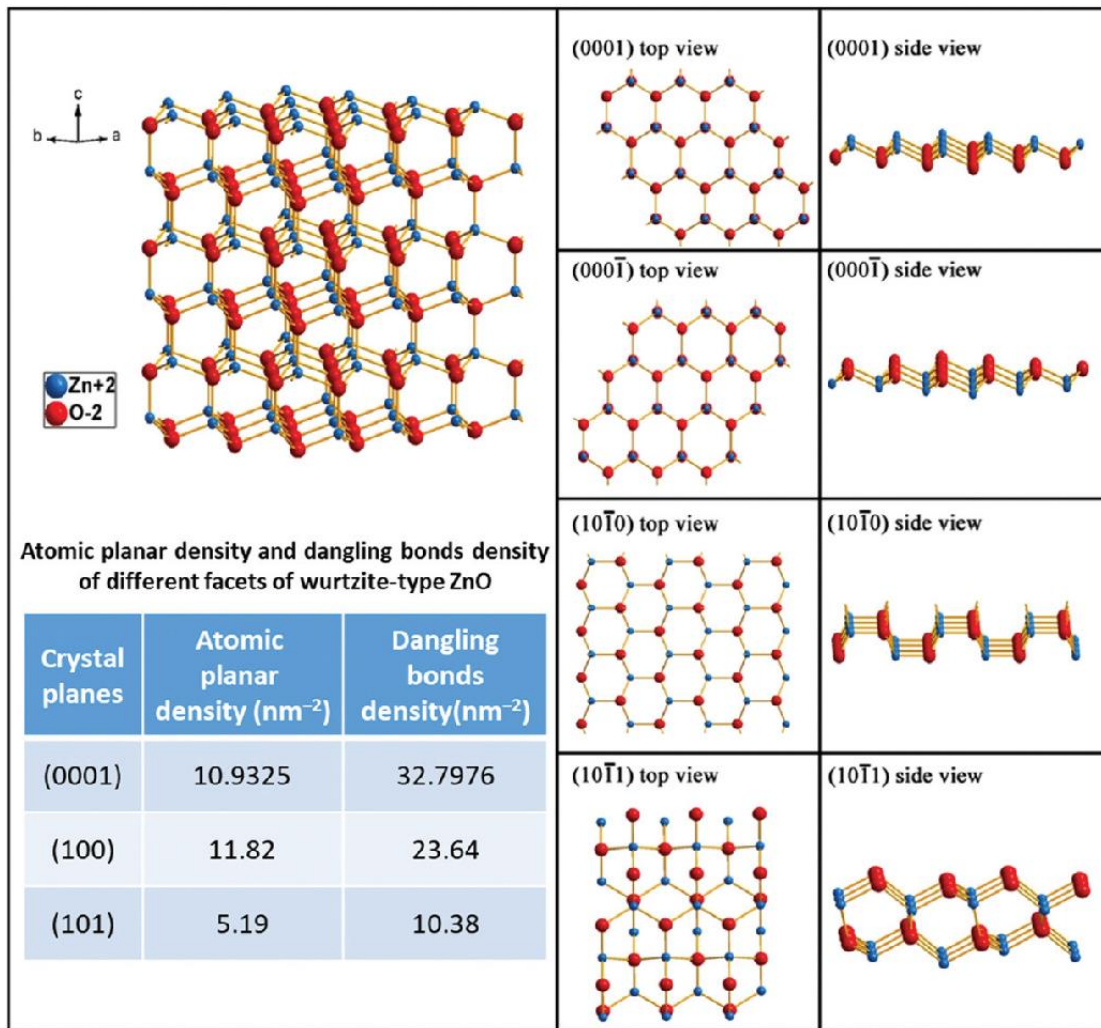
Figure 5 Wurtzite-type Zinc oxide atom packing system with information analytics [14].

2.2.2 Modification with noble metals

One effective and commonly used approach is catalysis chemical processes by using noble metals. The use of noble metal modification will improve the performance of metal oxide useful forms in a variety of ways. The most commonly employed base metals for dopants noble metals are gold, silver, platinum, and palladium, which can significantly increase the gas reaction for MOS gas sensing materials. While there are several cases that contain various situations, the following are some appropriate explanations: 1. The adsorption energy is diminished as many O⁻ and target gases are bound, 2. The charging clusters are dispersed, which allows the bands to stretch and create a Schottky barrier, which affects electron movement, and 3. The reaction's

absorption energy is decreased by the spillover effect. While this technique will greatly increase the gas adsorption efficiency of the metal oxide semiconductors, unfortunately, it may impact the price of the fabrication process to some extent and may raise the chances of material damage due to catalyst toxicity.

2.2.3 Alternative metal heteroatom doping

In particular, in several situations, heteroatom doping together with the other elements, in additional to noble metal modification, will greatly enhance the gas response of MOSs. Apparently, the main purpose seems to be to adjust the energy band structure of the material.

For certain situations, introducing heteroatoms to a metal oxide semiconductor substitutes the precursor metal atoms, resulting in smaller particle diameters. The entire particles would be occupied by the electron depletion layer whenever the particle size becomes less than double the Debye length, thus enhancing the gas sensing properties of MOS. Furthermore, experimentation has confirmed adjustments in the specific surface area and pore volume.

2.2.4 Oxide heterojunction fabrication

Heterojunctions are made by mixing 2 or several metal oxide semiconductor materials to gain additional benefits and improve detection sensitivity. This strategy can improve response. These explanations exactly suit the aforementioned gas sensing mechanisms. As compared to when the electron depletion layer is not doped, the electron depletion layer gets smaller, and the performance enhancement occurs as an improvement in the material conductivity on the macroscopic level. The transfer of electrons or holes happens in order to preserve equilibrium in the system.

2.3 Literature survey

Zinc oxide as a gas sensing material

From previous studies, it has been found that ZnO is a semiconductor metal oxide that has been interested in applying to be a gas sensor, such as the following research.

In 1998, P. Mitra et al. [15] have studied the gas detection capabilities of ZnO film produced by a chemical deposition process. This film can detect hydrogen gas at 3 vol%, which shows more response values. 90% at 150 ^{o}C. However, this sensor has a poor response/recovery time but this sensor will have a better response when tested with liquefied petroleum gas (LPG) at a concentration of 0.4-1.6 vol% with a response value of 50-75%, where a response value of 75% occurs at 300 ^{o}C. The sensor takes only 12 seconds to respond and recovery time was 4.5 minutes.

In 2005, Chu Xiang Feng et al. [16] invented the zinc oxide sensor from zinc oxide nano-tetrapods under 4 different atmospheres, which are under dry argon and dry nitrogen, humidified argon, and dry. It was found that the preparation of zinc oxide under the dry argon, tetrapod has a length of about 300 to 600 nanometers and a diameter of 20 to 100 nanometers and the length will decrease when preparing in humidified argon. In addition, the preparation of zinc oxide under nitrogen has the same tendency as argon preparation. The researchers used the prepared sensor to test C_2H_5OH vapor at 1000 ppm under 130-400 ^{o}C, it was found that the sensor prepared under the dry argon atmosphere had the highest gas response equal to 14.3 at an operating temperature of 130 ^{o}C. The sensors prepared under a humidified argon atmosphere have a maximum gas response of 130.7 at 300 ^{o}C. Sensors that are prepared under the dry nitrogen atmosphere have a gas response of 108.4 at 380 ^{o}C and the sensors prepared under humidified nitrogen atmosphere not responding to ethanol at temperature between 150-400 ^{o}C and in the same year, P.P. Sahay et al. [17] used zinc oxide thin film to measure ethanol at various operating temperatures. It was found that the film sensor detected ethanol at relatively high concentrations of 1,000 to 5,000 ppm at an operating temperature of 150-350 ^{o}C.

In 2006, J X Wang et al. [18] prepared a sensor to test carbon monoxide, ammonia, and hydrogen gas from a zinc oxide nanorod synthesized by the hydrothermal technique. Size of the zinc oxide nanorod is between 30 and 100 nm. According to the research, the sensor has the best response to hydrogen gas. When compared with the other two gases and showing the highest response at 250 ^{o}C at a gas concentration of 20 ppm, however, the prepared gas sensor is capable of detecting carbon monoxide and ammonia as well.

In 2008 Yu Jin Chen et al. [19] fabricated an ethanol sensor from zinc oxide nanotubes prepared with sonochemical method. The sensor produced has a high gas sensitivity at 300 ^{o}C, Ethanol gas can be detected at low concentration levels as one part per million.

Zinc oxide mixed with various substances

The gas response of the gas sensing devices could be developed by adding the substance to the zinc oxide sensor, such as the following research.

In 1998, N. Jayadev Dayan et al. [20] presented research on the detection of hydrogen, carbon monoxide and methane from pure ZnO and antimony-doped zinc oxide sensors. According to the gas test results, antimony-doped zinc oxide sensors show higher sensitivity than pure zinc oxide sensors, which depend on the amount of the catalyst and increase as the gas concentration increases.

In 1999, G.S.T. Ra O et al. [21] used a thick film from pure zinc oxide powder and doped with palladium, iron (Fe) and rubidium (Ru) to detect ammonia gas. The gas sensing devices were employed to notice the ammonia gas at the concentration of 30 ppm, the response of pure zinc oxide sensor, the palladium-doped zinc oxide sensor, iron-doped zinc oxide sensor and, the rubidium-doped zinc oxide sensor was approximately 35, 60, 25 and 10%, respectively. According to the results, Palladium-doped zinc oxide sensors provide fast sensitivity/response time to ammonia gas at room temperature, which takes only 4 seconds to respond with the ammonia concentration range of 30 ppm.

In 2000, F. Paraguay D. et al. [22] selected 5 catalysts for zinc oxide doping to fabricate a thin film for detecting ethanol gas, namely Al, In, Cu, Fe, and Sn, by doping each substance in amounts from 1, 3, 5, 7 and 15 at.% at operating temperature 675 K. The results found that at the appropriate amount of catalysts to detect 100 ppm ethanol concentration, the sensor showed the descending order sensitivity of the following: ZnO : Sn 0.4 at.%, ZnO : Al 1.8 at.%, ZnO : Fe 1.1 at.%, ZnO : In 6.5 at.%, and ZnO : Cu 3.6 at.%

In 2009, T. Nittaya et al. [23] studied the effects of the hydrogen gas response of 0.2-2.0% platinum-doped zinc oxide thick film prepared by with Spin coating technique on alumina substrate under operating temperature 200-350 $^\circ$C, it can be concluded that the thick film 0.2 at.% Pt/ZnO provides the highest response value, which is approximately 164 at the concentration of hydrogen is 1 volume% and at operating temperatures of 300 $^\circ$C.

Zinc oxide mixed with graphene

In 2011, Singh G. et al. [24] have studied the gas detection capabilities by using zinc oxide decorated graphene oxide sheets at 25 $^\circ$C. Results show that the detection of 22 ppm CO, 1 ppm NH_3, and 5 ppm NO have response values, response/recovery time that are 24.3%, 5/5 for CO, 24%, 6/3 for NH_3, and 3.5%,25/- for NO, respectively.

In 2014, Anand K. et al. [25] have studied the H_2 gas sensing device by using ZnO/graphene composite with sensors prepared from graphene oxide varied from 0, 0.6, 0.9, 1.2, and 1.5 wt%. The operating temperature used in the experiment is in the range of 100-450 $^\circ$C. From this research, it shows that the nanocomposite film has good response at lower temperatures compared to zinc oxide film. In addition, for the production of composite hydrogen sensors, an optimal volume of graphene material, i.e., 1.2 wt percent, has been proposed that provides the strongest detection against 200 ppm H_2 at 150 $^\circ$C,.

In 2014, He J. et al. [26] have fabricated rGO-ZnO composite from a 2 steps hydrolysis-calcination process. Results show that the composite provide large response,

and the sensor can detect 50.09 to 1000 ppm acetone with the optimal temperature of 260 ^{o}C. Furthermore, the crystallinity of reduced oxide graphene-Zinc oxide nanocomposites, instead of particle size, is the most essential property for gas response when used in gas sensors.

In 2014, Song N. et al. [27] were synthesized functionalized graphene/ZnO (FGZnO) nanohybrids by a modified in situ synthesis for ethanol gas sensor. The sensor can detect 100 ppm C_2H_5OH vapor at an optimum temperature of 340 ^{o}C with response 93.5% and response/recovery time is 5/20 s.

In 2017, Hyoun Woo Kim et al. [28] have considered the effect of microwave irradiation on the synthesis and treatment of ZnO/graphene for gas sensing applications. The sensing devices were put to the test against a variety of gases, and the findings were comparable to that of pure ZnO and ZnO/graphene sensors that had not been exposed to MW radiation. In contrast to untreated group nanocomposite and pure ZnO sensing material, the MW radiation detector had an even better sensitivity, especially to NO_2 gas (1 ppm NO2 at 300 ^{o}C provide a response value of 12.57), as well as better selectivity and faster response/recovery times.

In 2019, Wang H. et al. [29] have studied acetone vapor sensors based on graphene-like porous ZnO/graphene oxide by using wet-chemical method with an additional calcining treatment. The results show that the optimum calcination temperature was found to be 525 ^{o}C, response value of the sensor was 94 toward 100 ppm acetone and recovery time is 4 s at optimum operating temperature of 400 ^{o}C.

Computational studies on using ZnO as a gas sensing material

In 2002, Jon M. Matxian et al. [30] have studied the electronic excitation energy of Zn_iO_i (i=1-15) clusters by using Time-dependent density functional theory (TDDFT). The results show that the $Zn_{12}O_{12}$ is the most spheroidal cluster, this is consistent with what has been seen with tiny ZnO nanocrystals. Which provided the evidence that perhaps the substrate configuration of such tiny Zinc oxide nanoparticles may be similar to the surface pattern of the $Zn_{12}O_{12}$ cluster.

In 2015, Chen et al. [31] have studied the methane adsorption on graphene and other dopant (B, N, P, and Al) by employing DFT calculation. The findings indicate that the P- or Al-doped graphene have higher performance than the others. With an adsorption energy of -3.28 eV, Al-doped graphene is the right alternative for CH_4 sensor.

In 2016, G S Rao et al. [32] used DFT to examine the association of CO_2 with a currently created Zinc oxide monolayer in its pristine, imperfect, and functionalized form (substitution of one O atom with B, C, and N atom). The E_{ad} of carbon dioxide molecule over the surface is calculated to be -0.20 eV, and the largest adsorption energy is -1.77 eV for $ZnOB-CO_2$.

In 2017, Meng et al. [33] have studied the role of gas molecule numbers, numbers of layers, and composite of adsorbed targeted gas over honeycomb-like zinc oxide by using first principle calculation. The findings of the calculations show that the adsorption energy of all the chosen gas particles is sensitive to intensity and homolayer number, and that they seem to continue rising as the gas concentration decreases.

In Gholizadeh R. et al. [34] have studied N_2O adsorption on honeycomb-like zinc oxide mixed graphene by using DFT calculation. The horse-like(N-N-O) interaction with the substrate was already determined to be the steadiest adsorption form, with an E_{ad} of -0.27 eV, according to this research.

Thus, based on literature, doping or modifying the ZnO nanostructures with graphene is an effective approach in promoting the gas sensing capabilities of the substrate. Understanding of gas sensing mechanisms and quantifying the relevant processes at the atomic level of different ZnO/graphene nanocomposites continues to be a major need. In this regard, the calculations will be carried out using DFT in order to gain fundamental understandings and identify the potential ZnO/graphene nanocomposite as a sensing material candidate. In accordance with the computational results, the ZnO/graphene nanocomposite has been experimentally synthesized to justify the concentration of graphene in such the composite. The combined theoretical and experimental study could make a prominent contribution to the design and fabrication of the sensing device with high gas sensitivity and selectivity.

Chapter 3

Computational methodology (Density functional theory (DFT) study)

3.1 Theoretical background of DFT

3.1.1 Density Functional Theory (DFT)

When considering the nature of chemical reactions of molecules on the surface of materials, both statistical properties and dynamic properties are of concern. The results of solving the many-body Schrödinger equation can be used to derive such properties. To solve this complex equation physicists have used several strategies to approach this problem, starting with The Hartree-Fork approximation, which has led to the diversity of quantum chemistry models of the modern day [35]. All of those methods originated on the wave function; however, the amount of work required to compute and process the wave function grows rapidly as the amount of electron increases. As a result, they're only useful for situations with a minimal number of reactive chemical electrons. Hohenberg and Kohn presented the fundamental theorem of DFT in 1964. The transformation of wave function to ground-state density as the main parameter was the most important result. Therefore, this principle is based on a straightforward 3-D density function $n(r)$ rather than the wave equation, which is a multi-dimensional variable $\psi(r_1, r_2, \ldots, r_N)$. While using this procedure necessarily requires an estimation of the exchange-correlation function, it has proven to be so effective that it has become the basic way to collect ground-state parameters.

- Kohn-Sham equation

The time-independent, non-relativistic Schrödinger equation for the many-electron wave function (ψ) is the foundation of electronic structural theory.

$$E\psi = \hat{T}\psi + \hat{V}\psi + \hat{V}_{ext}\psi,$$
(3.1)

where $\hat{T}$ denotes the kinetic energy operator, $\hat{V}$ denotes the electron-electron interaction potential, and $\hat{V}_{ext}$ denotes any external field potential.

As Hohenberg and Kohn have primary demonstrated in their work [36], two objective maps exist;

$$n(\boldsymbol{r}) \to |\psi[n]\rangle \text{ and } n(\boldsymbol{r}) \to V_{ext}(\boldsymbol{r}), \tag{3.2}$$

that establishes one-on-one relationships here between ground-state charge density and the electronic wave function, along with the outward potential. The ground-state formulation of such Schrödinger equation could be found by decreasing the intensity of a trials ψ and employing Eq. (3.2) for the density of the charges, according to the Rayleigh-Ritz nonlinear theory.

$$E_0 = \min_{\psi}\langle\psi|T + V + V_{ext}|\psi\rangle = \min_{n(\boldsymbol{r})} E[n(\boldsymbol{r})], \tag{3.3}$$

where

$$E[n] = T[n] + V_H[n] + E_{xc}[n] + V_{ext}[n]. \tag{3.4}$$

$T[n]$ is the kinetic energy functional for non-interacting electrons and $V_{ext}[n]$ the functional of the outward potential. $V_H[n]$ represents the practical of the classical Coulomb interaction energy, i.e., the Hartree energy, is represented by

$$\frac{1}{2} \int d\boldsymbol{r}d\boldsymbol{r}' \frac{e^2}{4\pi\varepsilon_0} \frac{n(r)n(r')}{|r-r'|}. \tag{3.5}$$

The electron density is usually written as a total of imaginary single-particle states to solve Eq. (3.3).

$$n(r) = \sum_{i=1}^{N} |\varphi_i(\boldsymbol{r})|^2, \tag{3.6}$$

with N represents the complete number of electrons. The series of Kohn-Sham equations [37] is then obtained by integrating the extension into Eq. (3.3) and reducing this under the condition that all φ_i are uniform and orthogonal to one another.

$$\left[-\frac{\hbar^2}{2m}\nabla^2 + V_{eff}(\boldsymbol{r})\right]\varphi_i(\boldsymbol{r}) = \varepsilon_i\varphi_i(\boldsymbol{r}).$$ (3.7)

The effective potential, $V_{eff}(\boldsymbol{r})$, is provided by

$$V_{eff}(\boldsymbol{r}) = V_H(\boldsymbol{r}) + V_{xc}(\boldsymbol{r}) + V_{ext}(\boldsymbol{r}).$$ (3.8)

The operational derivative of the mathematical exchange-correlation of regard to the density of charges is $V_{xc}(\boldsymbol{r}) = \frac{\delta E_{xc}(\boldsymbol{n})}{\delta n}$. Which series of solitary coupling formulas is nearly similar to what can be obtained using the basic Hartree approximation, which helped identify the many-electron wave equation as just a result of solitary φ,

$$\psi(\boldsymbol{r_1}, \boldsymbol{r_2}, \dots, \boldsymbol{r_N}) = \varphi_1(\boldsymbol{r_1})\varphi_2(\boldsymbol{r_2})\cdots\varphi_N(\boldsymbol{r_N}).$$ (3.9)

The Kohn-Sham solutions are obtained again after combining the result frequency with the previous one to obtain a better approximation of the accurate charge density. That process is reproduced till a converged charge density is obtained. The self-consistency loop will be the name of this procedure. Eventually, the ground-state energy is calculated using the self-consistent charge density,

$$E[n] = \sum_{i=1}^{N}\varepsilon_i - \frac{1}{2}\int d\boldsymbol{r}\, V_H(\boldsymbol{r})n(\boldsymbol{r}) - \int d\boldsymbol{r}\, V_{xc}(\boldsymbol{r})n(\boldsymbol{r}) + E_{xc}[n].$$ (3.10)

- Exchange-Correlation Functionals

The right manner of the exchange-correlation function, $E_{xc}[n]$, can be used to answer the Kohn-Sham equations, Eq. (3.7). The many-body quantum-mechanical effect are included in this function, which is not well known in a confined and empirical manner.

The functional exchange-correlation (LDA) is the first effort to get a true description of the exchange-correlation functional [38]:

$$E_{xc}[n] \approx \int d\boldsymbol{r}\, n(\boldsymbol{r})\, \varepsilon_{xc}\big(n(\boldsymbol{r})\big), \qquad (3.11)$$

where $\varepsilon_{xc}(n(\boldsymbol{r}))$ is the exchange-correlation energy per atom. The functional exchange-correlation function is therefore an entirely internal function which just depends mostly on intensity at direction $\boldsymbol{r}$,

$$V_{xc}^{LDA}(\boldsymbol{r}) = \frac{\partial}{\partial n} n\varepsilon_{xc}(n)\bigg|_{n=n(\boldsymbol{r})}. \qquad (3.12)$$

The exchange-correlation energy can be calculated and normalized employing an approximation framework based on the homogeneous electron gas from quantum Monte Carlo calculations [39] that interpolates between analytical asymptotic behaviors and intermediate effects. The LDA also provides very good results for constants of the lattice and geometric arrangements.

The gradient of the density must be used in the approximation in order to enhance the precision of the estimation to a level that is appropriate to surface science complications involving the measurement of thermodynamic electrical structures of inhomogeneous frameworks. However, the direct extension of the exchange-correlation functional was usually frustrating when introduced to actual structures, since the shortened sequence breaks essential physical characteristics including the absolute law for the exchange-correlation gap [40]. That is resolved when constructing the generalized gradient approximation (GGA), in which the functional exchange-correlation is described as,

$$E_{xc}[n] = \int d\boldsymbol{r}\, n(\boldsymbol{r})\, \varepsilon_{xc}(n(\boldsymbol{r}), |\nabla n(\boldsymbol{r})|). \qquad (3.13)$$

Common growing properties and approximation actions of efficient potential are achieved by following and allowing the use of correct sum laws. Within semi-local GGA functionals, binding energies are greatly increased, and for several nanoparticles, the total error should be less than 0.3 eV [41]. Generalized gradient approximation in the shape presented by the Perdew-Burke-Ernzerhof functional (PBE) was used to perform all of the calculations in this analysis [42].

- Plane Wave Basis Sets

In the previous section it was shown that Eq. (3.1) has provided the many-body problem that can be converted efficiently to a series of quasi-single particle formula, Eq. (4.7). Nonetheless, deriving that Kohn-Sham formula leaves a difficult challenge for such system of solid states [43]. For a periodic method, however, the standard solution is to extend the quantum state into a series of distinct plane wave bases.

$$\varphi_{k,i}(r) = \sum_G c_{i,k+G} e^{[i(k+G)\cdot r]},$$
(3.14)

with G denotes the vectors of the reciprocal lattice and k denotes the first vector that lie inside the first Brillouin zone. Bloch's theorem now provides the model for plane waves, as seen in Eq. (3.14). For intensive reasons, at any kinetic energy cut-off the expansion must be limited at each *k-point*,

$$E_{\text{cutoff}} = \frac{\hbar^2}{2m} |k + G|^2.$$
(3.15)

So, the accuracy of this calculation can be managed easily by extending E_{cutoff}.

For an infinite solid there is infinite number of *k-points*. Since any occupied state contributes to the electrostatic potential at any given *k-point*, The Kohn-Sham formulas must be solved employing an endless number of plane-wave extensions throughout the format of Eq (3.14). In particular, the φ at *k-points* close together should be approximately equal, implying that the total wave function will be defined by a limited

number of *k-points*. When selecting this set *k-point*, exploiting fundamental symmetries and minimizing every integration to the irreducible portion of its Brillouin zone is optimal. The groups of specific k-points initially mentioned by Monkhorst and Pack [44], that comprise basically about an equispaced *k-point* array, are the most common. Therefore, every expectation value can be measured,

$$\langle X \rangle = \frac{1}{V} \int dk X_n(k) f(\varepsilon_n(k)),$$

(3.16)

displacing the integral with such a limited summary of such selected *k-point* set, and providing the integral over the reciprocal unit cell volume *V* and the summary over whole bands *n*. An enhanced interpolation system including the linear tetrahedron approach [45] is used to increase the precision of this discrete estimation to integration of the Brillouin zone. For surface science questions, one *k-point* in the usual path to the layer is appropriate since in this path no periodicity is presumed, and hence no band dispersion. Thus, an expanding technique is widely used, while interpolation approaches will need more than one *k-point* to be employed in each direction.

Use an extension of a plane wave, Eq. (3.7) is transformed to matrix equation,

$$\sum_{G'} \left[-\frac{\hbar^2}{2m} |k + G|^2 \delta_{GG'} + V_{eff}(G - G') \right] c_{i,k+G'} = \varepsilon_i c_{i,k+G},$$

(3.17)

where $V_{eff}(G - G')$ is the Fourier transform of the effective potential, and the kinetic energy is given as a diagonal.

- Pseudopotential Approximation

A discrete group of plane waves is employed to generalize the wave functions within the context defined in the preceding subsection. While Bloch's theorem ensures the merging of extension, nevertheless, this method is quite insufficient to explain the very densely bound core e$^-$ with their extremely oscillating φ.
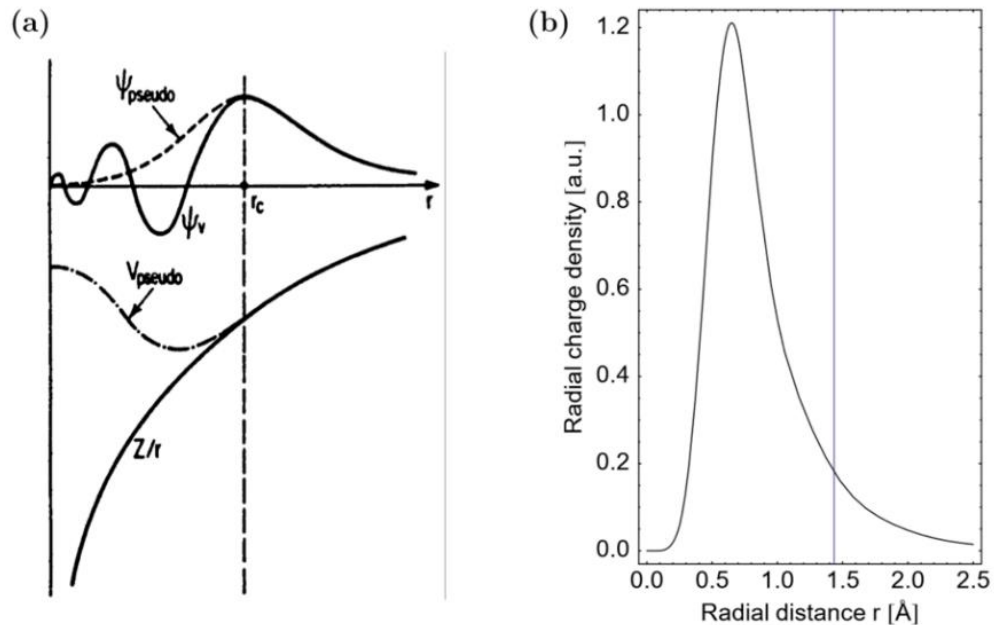
Figure 6 (a) Pseudopotential approximation schematics. The pseudo equivalents of the potential all-electron (black lines) and φ (dot line) are used instead. The core radius [46], is the radius of which the two points are related. (B) The valence palladium electrons' pseudo charge density. At the core radius is 1.434 Å.

This basic approach is seen in Fig. 6(a): Both the pseudopotential and the pseudo-φ outside the core radius, r_c, are similar to the real potential and φ. For instance, for palladium, the number of electrons to be manipulated in the equation is decreased from a total of 46 electrons to 10 d Pd electrons. Some other solution to disentangling core and valence states is the method known as the augmented-wave projector (PAW) [47]. For most structures in which the dispersal of the charge density strongly matches that of the isolated atom mention system inside the core region. The PAW approach is particularly effective for complex with large magnetic moments, whereby atomic coupling energy are sensitive to core charge density.

- Supercell

In order to use Bloch's theorem and a plane wave base set, the issue must be periodic in all 3-D. This is obviously accomplished for measurement of bulk metal.

Nevertheless, by adding a surface, periodicity is eliminated in one direction. If the substrate is regular in the axis of z, there will be a semi-infinite bulk area and a semi-infinite vacuum area along the z direction, with the x-y plane retaining periodicity [48]. Nonetheless, throughout the slab strategy, each slab of 2 surfaces and a limited layer thickness substitutes the semi-infinite metal. And one possesses a two-dimensional lattice in which the surface unit cell provides the periodicity. In order to restore the 3-D periodicity, the slab is replicated in the z-axis by introducing a relatively huge area of space between them as seen in Fig. 7.
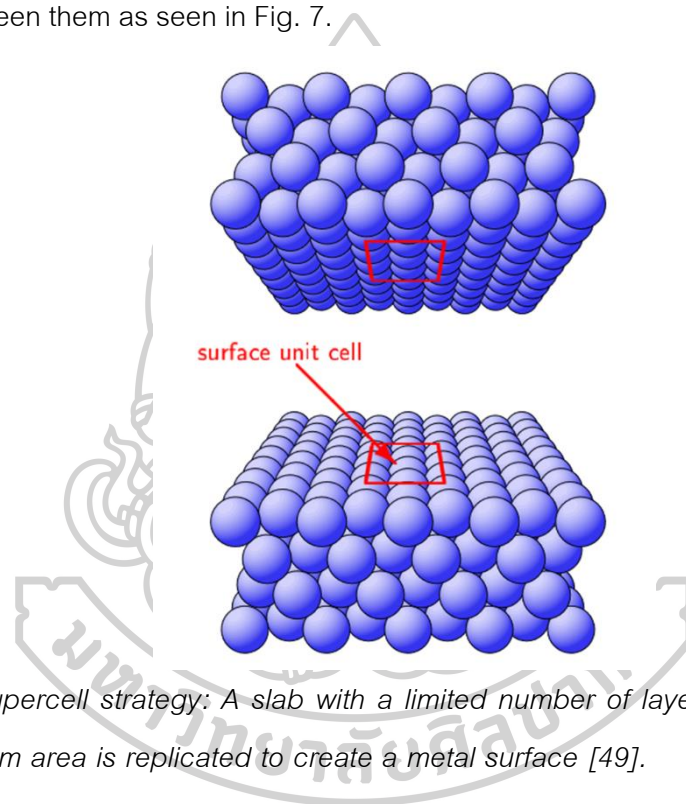
Figure 7 Supercell strategy: A slab with a limited number of layers and a reasonably large vacuum area is replicated to create a metal surface [49].

After all, one needs to verify whether this simulated, supercell is always similar to physical existence: the vacuum area must've been wide enough ($\Delta z \geq 10 \text{Å}$) to distinguish all slab surfaces to prevent any encounters with opposing surfaces or adsorbents. Four or more strata are now appropriate for low-index metal surfaces to reach convergence. Lastly, the substrate unit cell's scale must have been defined in this way which it correlates with analytical model coverages or is wide sufficient to exclude spatial adsorbent interactions.

3.1.2 Calculation of Physical and Electrical Properties using DFT

A broad variety of surface science problems can be solved using the computational approaches mentioned coupled with existing computing resources. Any of these characteristics, such as adsorption energies or work function shifts, are closely comparative with scientific results, which aids in the validation of research observations.

- Geometry relaxation

An accurate surface model needs to be used to better explain chemical reactions at interfaces. Having used the slab method, there is easily an absolute measure in the substrate. Because of a multi-layer sufficiently slab and vacuum region, the bulk properties of the metal being studied may also be replicated.

The selection of the bulk lattice constant is the first serious component when constructing the slab model. Numerically, calculating the cohesion energy's exact energetic minimum according to the lattice constant is very complicated.

Then the surface slab is created as a second step, the inclusion of 4 or 5 bulk layers is normally enough. On certain metal structures, this results in the first surface layer relaxing inwardly. And the slab layers have to be relaxed for a reliable surface model. The ionic forces calculated will effectively do this and thereby refining the geometric configuration of the slab substrates till the energetic reduction is reached and, equally, a force-free condition.

Unless the adsorption mechanism is asymmetrically configured anyway, the precision of the slab model can be increased by having the layers on one side of the slab locked at their bulk location. Only the "top" half of the substrates of the slab enable relaxation. While this compromise a clear definition of the surface morphology with one side, it significantly improves the description of the sub-surface layers.

The precision of geometric data is now reasonably decent even though using approximation of local-density alone. In addition, geometric estimates are reasonably comparable with the experimental results collected.

- Adsorption energy and potential energy surfaces

The charge carriers of the reactant are often claimed to be in their corresponding lowest energy and adiabatically accompany neighboring nuclei in density functional theory approach of chemical processes [50].

Because of these restrictions, the total DFT energy is normally received, *E[n]*, per supercell at a specified range of ionic coordinates, *(R_l)*. The change in total energy of the adsorbed complex and the total energy of the isolated cleaned layer and the adsorbent is then the energy of adsorption per adsorbent. This gives an example, for H_2 adsorption on Pd(100),

$$E_{ads} = -(E[H_2/Pd,Zn(100)] - E[Pd,Zn(100)] - E[H_2]).$$
(3.18)

By using description, greater positive energy from adsorption processes implies a more attractive reaction between the substrate and the adsorbent. In the case of atomic adsorption, careful attention must be given to where the energy relation for the separate system is located. The E_{ads} per adsorption molecule for atomic hydrogen adsorption will be calculated as

$$E_{ads} = -\left(E[H_2/Pd,Zn(100)] - E[Pd,Zn(100)] - \frac{1}{2}E[H_2]\right).$$
(3.19)

Therefore, the expense of splitting the bond of the stable H_2 molecule is already included in the gas phase. If the results of E_{ads} from Eq. 3.19 is not negative, adsorption and dissociation in thermodynamic equilibrium is vigorously optimal for an H_2 molecule.

E_{ads} also cannot provide a complete image of the adsorption mechanism [51]. Except though dynamic simulations of the adsorption mechanism are not carried out, it is beneficial to approximate the adsorbate's potential energy as a function of the nuclei's coordinates employing DFT. A scalar function of most ionic coordinates is the potential energy surface (PES), is labeled this quantity, *E(R_l)*. For measurements of adsorption, it

is always common to conclude that the layer is inflexible and that its optimization is insignificant in the adsorption mechanism.

- Charge density analysis

For any study of the chemical interactions, the most clearly accessible quantity is the charge density, becoming the central component of mass-functional theory. The production of bonding and anti-bonding levels would be specifically expressed as an aggregation or depletion of electrons in the e⁻ density, $n(r)$. This is demonstrated on Fig. 3.3 (a) for the basic case of an individual H_2 molecule: the aggregation of charges between the 2 H_2 is distinguished owing to the creation of the σ orbital bonding.

Relocations of the charge density are not as readily evident with more complex forms. Considering the disparity in e⁻ density of the coupled and uncoupled model is far more important in this case. In theory, "switch off" the contact between, such as, an adsorbent and the surface does not cause any difficulties. The charge densities of the adsorbent and the surface can be conveniently measured independently, except the locations of the connecting adsorbate-substrate structure. The difference in e⁻ density can be conveniently calculated as

$$\Delta n = n(interacting\ system) - \sum_i n(non-interacting\ subsytem\ i). \quad (3.20)$$
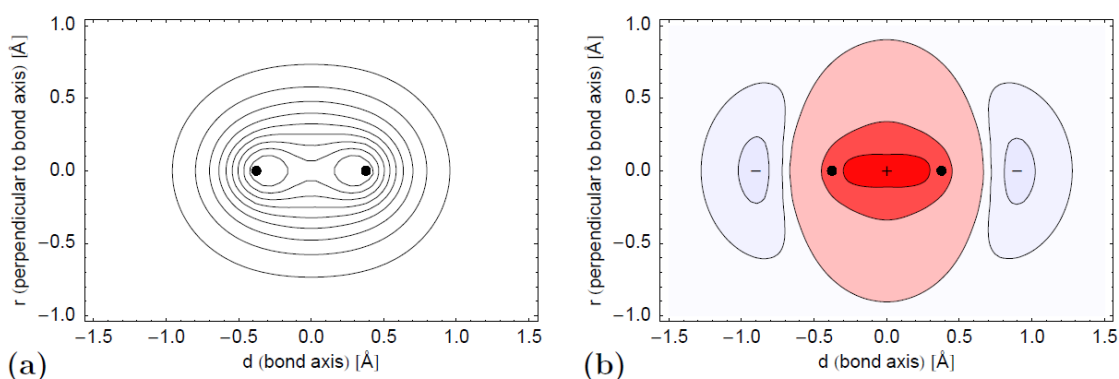
Figure 8 (a) H_2 molecule charge density diagram obtained under GGA approximation. The nucleic locations are labelled with dots. The contour lines have been drawn at 10, 20, …, 90 percent of the density of the full charge. (B) Differential density diagram of

the H₂ molecule compared to two non-interacting H₂ molecule; Electron charging
spreads from external (-) regions to bond (+) regions. The contour districts are called
at a minimum or maximum difference level of 50 percent and 90 percent respectively
[52].

The corresponding density disparity is shown in Fig. 8(b) for bonding of the H_2, at which two non-interacting components are the 2 H atoms. The charge aggregation is now plainly apparent in the bonding area, but rather the charge reduction of the σ^* orbital to the both side of the H atoms. And therefore, it is able to discover some relation in actual space and acquire an understanding about the interactive system's caused charge redistributions and hybridizations.

- Density of states

The density of the states can be determined by observing at it (DOS), an additional detailed sight of the relationship of each adsorbent with its surface is probable. This quantity is fully available in density functional theory approach, and is described as

$$N(E) = \sum_{i=1}^{\infty} \delta(E - \varepsilon_i).$$

(3.20)

In which the sum expands to all eigenstates of the Kohn-Sham Hamiltonian, Eq. (3.7). This distribution is typically smeared out for a calculation with a limited number of eigenstates to produce a constant dispersal suitable for a bulk substance, for example using a Gaussian or Methfessel-Paxton smearing [53]. Total density states calculated using Eq. (3.20) is composed of all electrons in the system. That being said, we are usually concerned about what occurs to the electrical orbitals of the straight involving orbitals of such adsorbent and the substrate associates in a bond destroying and construction mechanism. Plenty of the time, the total density of states can't easily define this detail. Therefore, it is beneficial to break down the density of state into its "building

bricks,", for example, the orbitals of the atomic valence. It could be accomplished by measuring the state-resolved or projected DOS as described by [54]

$$n_\alpha(E) = \sum_{i=1}^{\infty}|\langle\phi_\alpha|\varphi_i\rangle|^2\delta(E - \varepsilon_i),$$ (3.21)

where ϕ_α is a suitably selected localized function. The φ is normally shortened to a sphere nearby an atom on a plane wave basis and then projected onto the corresponding atomic s, p, and d orbitals [55]. When this dissection happens, the origins of binding and anti-bonding recombination orbitals could be referred to the atomic origins.

3.2 Computational details

The Vienna ab initio simulation package (VASP) was employed to operate first-principles computations based on density functional theory (DFT) [55, 56]. For calculating the exchange-correlation function, the generalized gradient approximation (GGA) in the format of the Perdew-Burke-Ernzerhof (PBE) functional was introduced [42]. The geometric relaxation and energy computation convergence conditions were set as follows:

(a) The cut-off energy was 450 eV

(b) The force on each atom is less than -0.01 eV/Å between two ionic steps

(c) The convergence of the electronic self-consist energy was less than 10^{-6} eV.

To superior explain the Van der Waals interaction, the long-range dispersion correction through Grimme's scheme [57] (DFT-D2) was employed all over the computation. The selection of the Brillouin zone has been conducted by the Monkhorst-pack scheme with a $5 \times 5 \times 1$ k-mesh for geometry relaxation and $9 \times 9 \times 1$ k-mesh for electronic structure calculations [44]. The Bader charge analysis was employed to investigate the charge transfer property between the gas molecule and the substrate [58]. The surface model then uses the vacuum region 25 Å.

The investigation of the absorption of gas molecules on metal oxide layer has been widely researched both experimental and computational. Theoretical studies for the absorption of gases on the zinc oxide surface that appear are mostly considered in a plane $(10\bar{1}0)$ [59] which is a predominant plane when coating zinc oxide film, yet a plane (0001) is another dominant and more sensitive than a plane $(10\bar{1}0)$ [60]. Therefore, the plane (0001) is another system that should be studied.

3.2.1 Substrate preparation

- graphene/ZnO and ZnO/graphene composites

First, the initial structures of bulk wurtzite ZnO and graphite were imported from literature and optimized. Then, a single ZnO layer was cut along the (0001) direction of the bulk wurtzite. Subsequently, the 6×6 ZnO surface (36 zinc atoms and 36 oxygen atoms) was fully relaxed and optimized. Afterward, an optimized 8×8 graphene monolayer containing 128 carbon atoms was used to match a 6×6 stoichiometric ZnO layer. Together, the hybrid nanostructure was created and performed the geometry optimization.

- graphene/ZnO nanocluster

Initially, the $Zn_{12}O_{12}$ nanocluster was created by cutting 8 hexagons from ZnO (0001). After that, adjust all the hexagons to connect with each other's (6 squares will appear). Then, $Zn_{12}O_{12}$ nanocluster was optimized and placed on an optimized 8×8 graphene monolayer to avoid interaction between $Zn_{12}O_{12}$ nanocluster with adjacent cells.

3.2.2 Initial condition of Gas adsorption on graphene, ZnO, graphene/ZnO, ZnO/graphene, graphene/ZnO nanocluster: H_2, CH_4, and N_2O gas molecules

We study the adsorption mechanism of H_2, CH_4 and N_2O gas molecules on pristine graphene, pristine ZnO, graphene/ZnO, ZnO/graphene, and graphene/ZnO nanocluster surfaces. For the most favorable complex, we consider all the possible adsorption points of the gas molecule over the substrate with various orientations. We

have placed gas molecules on the diverse adsorption points of each substrate, in which each substrate has a different adsorption sites as follows:

1. For graphene, there are 3 adsorption sites which are above C, bond, and hollow as is the Fig. 9

2. For ZnO, there are 4 adsorption sites which are above Zn, O, bond, and hollow as is the Fig. 10.

3. For ZnO nanocluster, there are 10 adsorption sites which are (above Zn, O, bond, and hollow of the first hexagon), (above Zn, and O of the square), (above the hollow of the second hexagon), and (above Zn, O, and hollow of the third hexagon) as is the Fig. 11.

Which for each gas will have different orientation depending on the molecular shape of that gas, which are

1. For hydrogen gas (H_2) which has molecular geometry in linear will be placed vertically and horizontally over different adsorption sites of each substrate.

2. For methane (CH_4) which has molecular geometry in tetrahedral will be placed by 1, 2, and 3 H molecules toward the different adsorption sites of each substrate.

3. For nitrous oxide (N_2O) which has molecular geometry in linear will be placed twice vertically and horizontally over different adsorption sites of each substrate (the second will be opposite with the first) because the N_2O gas molecules are asymmetric.

The different initial conditions of the gas adsorption process will give the results differently in the physical characteristics of the structure, the bond length, or the adsorption energy. Since the adsorption system can be defined in many ways, we have defined the initial condition of the adsorption system to cover all possible forms, making the calculated data very large. Therefore, only the part that has the best form of so theadsorption process in each system will be studied.
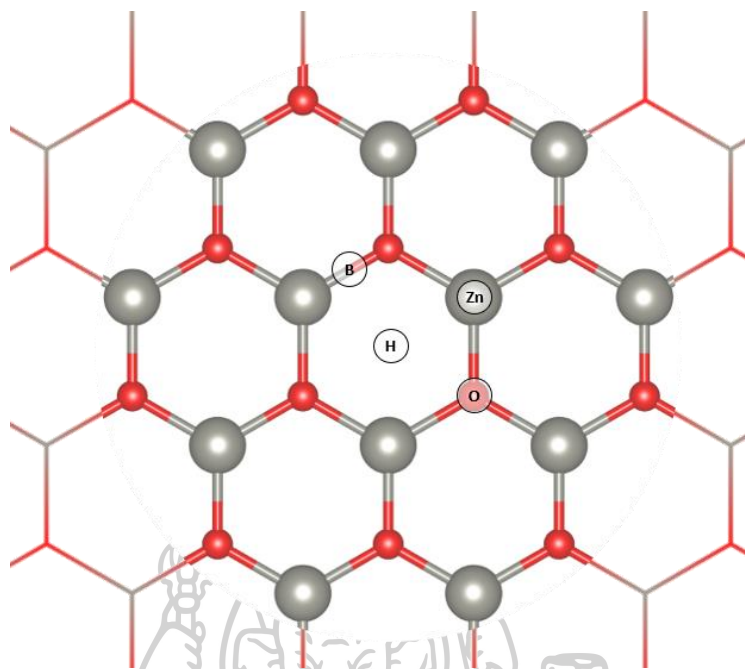
Figure 9 Four initial adsorption sites of monolayer honeycomb-like ZnO absorbent.
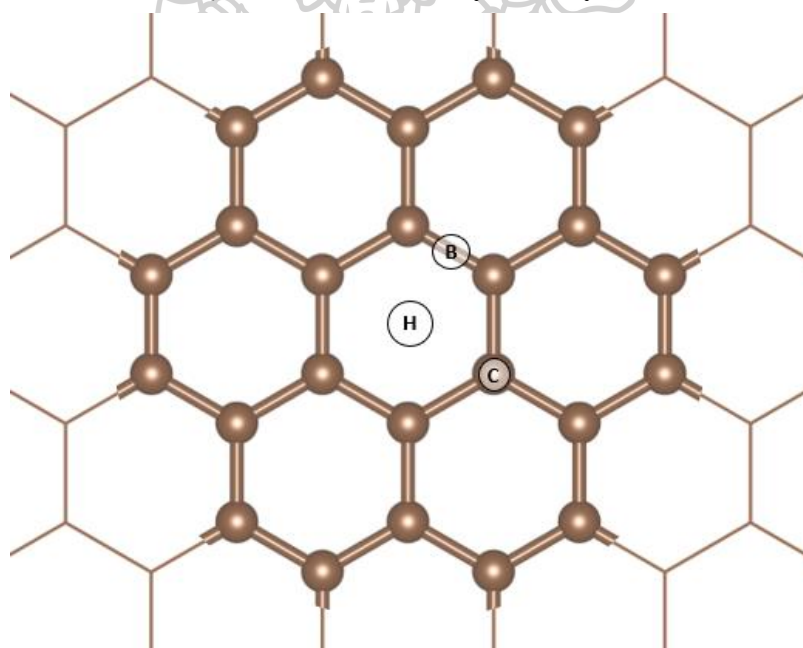
Figure 10 Three initial adsorption sites of monolayer graphene absorbent.
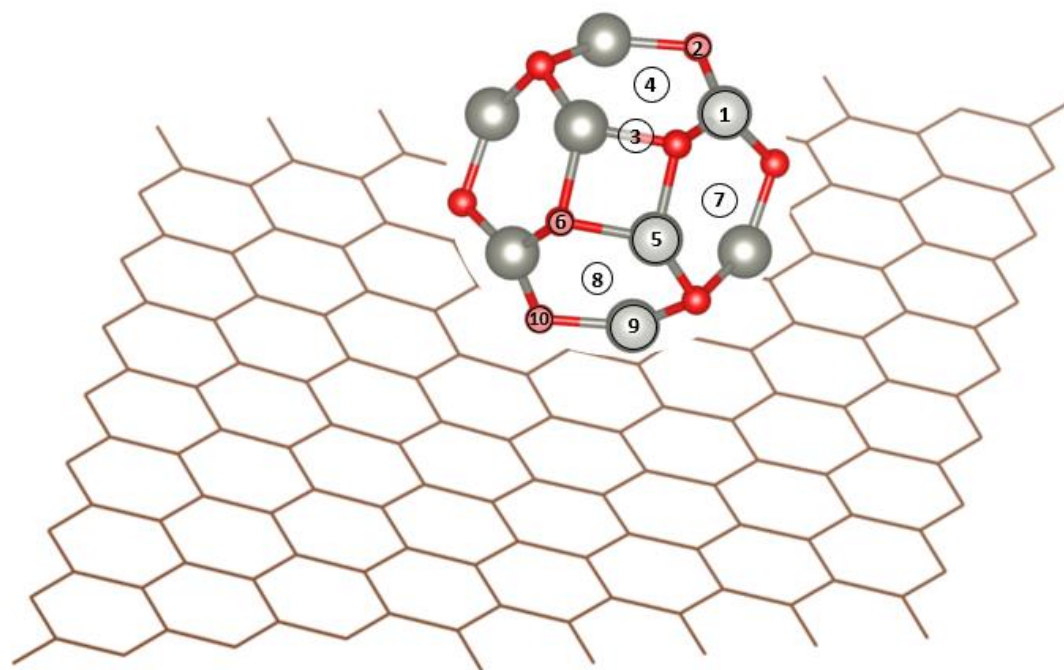
Figure 11 Ten initial adsorption sites of ZnO nanocluster on monolayer graphene absorbent.
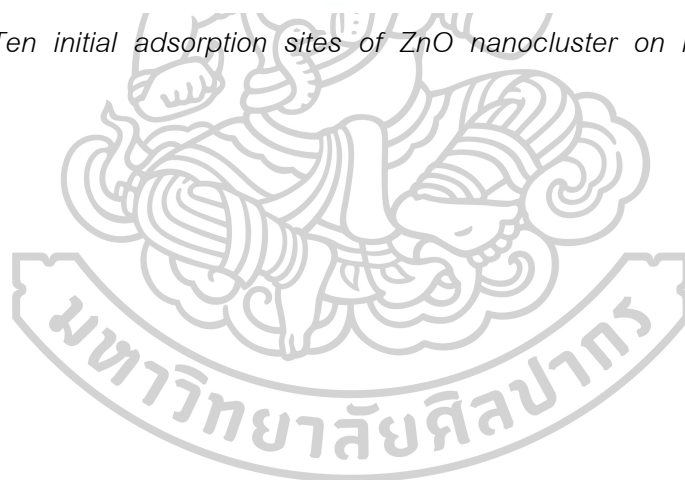
Chapter 4

Experimental methodology

In this chapter, ZnO nanoparticles were prepared through the precipitation method and graphene powder was prepared by the one-step electrolytic exfoliation method. Then selected batches of synthesized solids were characterized by FEG-SEM, XRD, Raman, UV-vis, and FTIR. Subsequently, sensor films from various amounts of graphene-mixed zinc oxide nanoparticles were fabricated by spin coating techniques. Finally, the gas response of such sensors was tested using the flow-through technique.

4.1 ZnO, graphene, binder preparation and sensors fabrication

4.1.1 Zinc oxide nanoparticles preparation

2.9749 g of Zinc nitrate hexahydrate ($Zn(NO_3)_2.6H_2O$, 98%, LOBA CHEMIE) was added into different ethylene glycol (EG, ≥99.5%, Fisher) solutions

1.) 100 ml of Ethylene glycol can be denoted as ZnO_100EG

2.) 75 ml of Ethylene glycol and 25 ml of distilled water can be denoted as ZnO_75EG

3.) 50 ml of Ethylene glycol and 50 ml of distilled water can be denoted as ZnO_50EG

4.) 25 ml of Ethylene glycol and 75 ml of distilled water can be denoted as ZnO_25EG

5.) 100 ml of distilled water can be denoted as ZnO_0EG.

Then the solution was heated to 60 ^{o}C and stirred for 30 min. Subsequently, 0.1 M of sodium hydroxide (NaOH, >99.0%, Fluka^{TM}) was added into the mixture until pH=7. After further stirring for 30 min, ZnO nanoparticles were collected by centrifugation at 10,000 rpm for 2 minutes and washed with distilled water twice to remove the excessive NaOH. The washed products were dried in an oven at 60 ^{o}C for 24 hours to obtain ZnO nanoparticles [61].
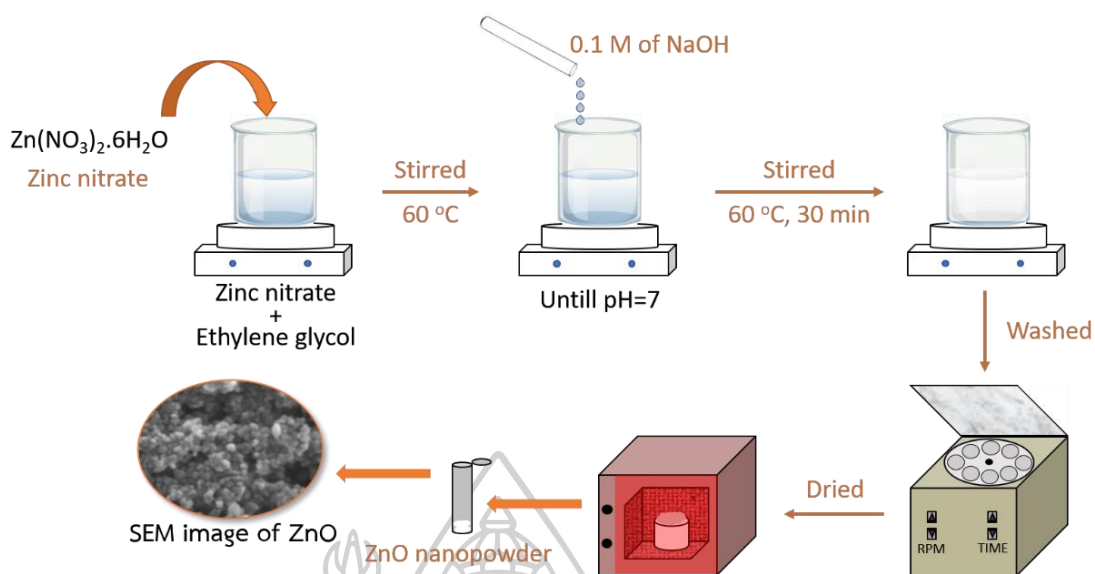
Figure 12 The synthetic method used to produce ZnO nanoparticles is depicted schematically in this diagram.

4.1.2 Graphene preparation

Graphene powder was synthesized in a Poly(sodium-4-styrenesulfonate) (PSS, M_w~70,000, Aldrich] solution by one-step electrolytic exfoliation, based on related procedures previously described [62]. In an electrochemical system filled with the PSS electrolyte (0.001 M of Poly(sodium-4-styrenesulfonate in de-ionized (DI) water), two high purity graphite rods [6 mm, 99.999%, Aldrich] were installed. A constant voltage of 8 V (direct current voltage) was installed between 2 electrodes for 24 hours. Then, the graphene powder was extracted from the solution by washing several times in ethanol and deionized water and drying at 80 $^\circ$C for 2 hours. A diagram of the synthesis apparatus is represented in Fig. 13.
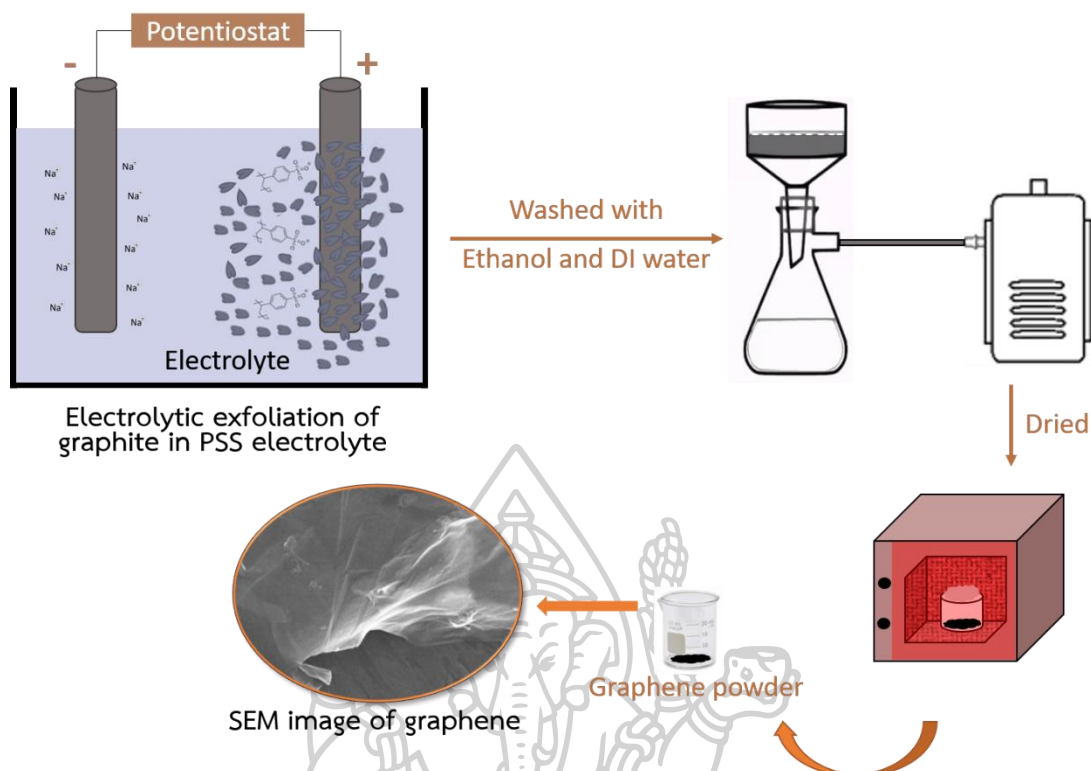
Figure 13 Diagrammatic illustration of the synthetic procedure employed for the preparation of graphene powder.

4.1.3 Binder preparation

18 g of Ethyl cellulose [SIGMA] was added into 480 mg of α - terpineol [97+%, ACROS Organics[TM]] at 80 $^{\circ}$C. After stirring for 4 h, the products were left to cool at room temperature and stored in the container.
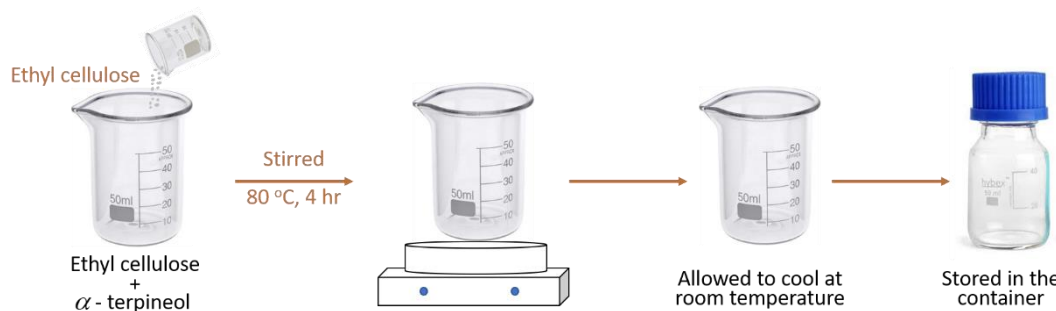
Figure 14 The synthetic process for the preparing of binder is depicted schematically.

4.1.4 Film sensor fabrication

Preparation of film sensors from various amounts of reduced graphene oxide-mixed zinc oxide nanoparticles using spin coating techniques.

1. Clean a glass slide thoroughly. Then, place three Al_2O_3 substrates with predeposited interdigitated Au electrodes of 0.30×0.40 square centimeters in width and length (Fig. 15(a)) on the glass slide. Then use transparent tape to attach the three electrodes on both sides of the electrodes, without letting the electrodes and the glass slide apart (Fig. 15(b)).

2. Prepare the mixed solution in clean room by weighing zinc oxide nanoparticles and measuring binders in the amount of 30 mg and 0.15 ml respectively. Put both substances into the mortar and mix it for 30 minutes (Fig. 16(a))

3. Place the glass slide attached with the prepared electrodes on the spin coater (Fig. 16(b)). After that, wipe the mixed solution on the electrodes and begin spin coating in 2 modes, 700 rpm and 3000 rpm for 10 seconds and 30 seconds, respectively.

4. Place the glass slide attached with the prepared electrodes on a hot plate (Fig. 17(a)) at a temperature of 90 $^\circ$C for 5 minutes.

5. Repeat step 3.-4. again, to create sensors with increased film thickness.

6. For the preparation of graphene-mixed zinc oxide sensors in the amount of 1, 5, and 10 %W/W can be prepared according to step 1. - 5. but changed from pure zinc oxide nanoparticles to graphene-mixed zinc oxide nanoparticles in the amount of 1, 5, and 10 %W/W.

7. The films were then annealed at 450 $^\circ$C using three-zone tube furnace (Fig. 17(b)) for 3 hr. at rate of 2 $^\circ$C/min for binder elimination.

8. After that, the prepared sensors after annealed were tested the gas measurements.

Remark: 10, 5, and 1 %W/W of graphene mixed with zinc oxide can be denoted as 10%Gr/ZnO, 5%Gr/ZnO, and 1%Gr/ZnO, respectively. And 0 %W/W of graphene mixed with zinc oxide can be denoted as ZnO.
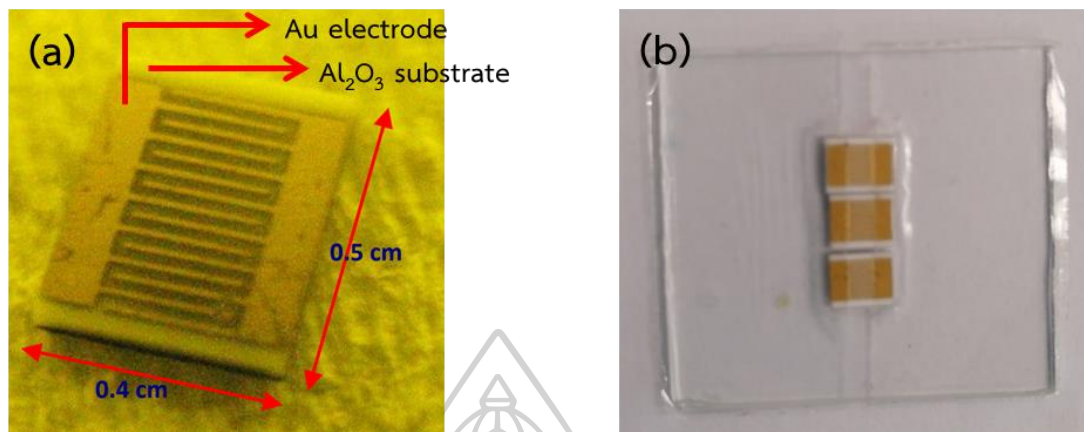
Figure 15 (a) Electrode prepared from the printing of Au electrode on alumina substrates. (b) Attaching the transparent tape on both sides of the electrodes over the glass slide.
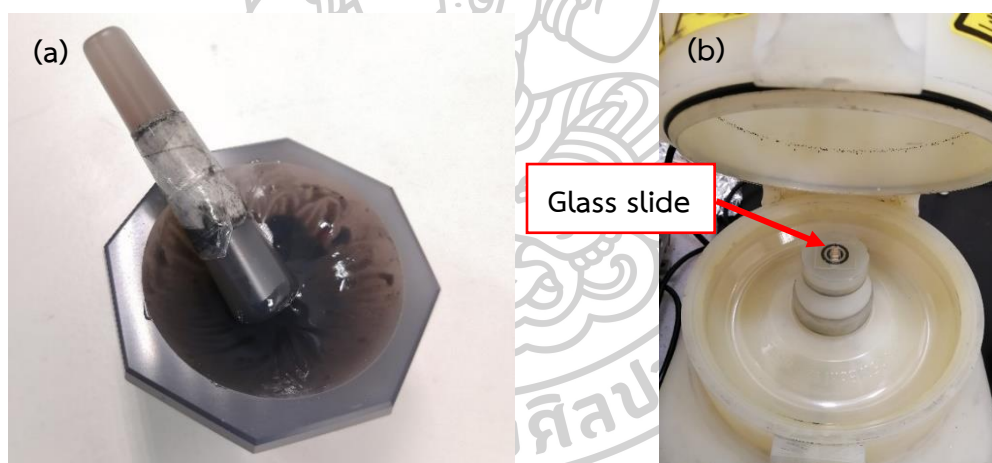
Figure 16 (a) Mixing of binders with graphene-mixed zinc oxide nanoparticles inside a pestle for preparing a mixed solution. (b) the glass slide attached with the prepared electrodes on the spin coater.
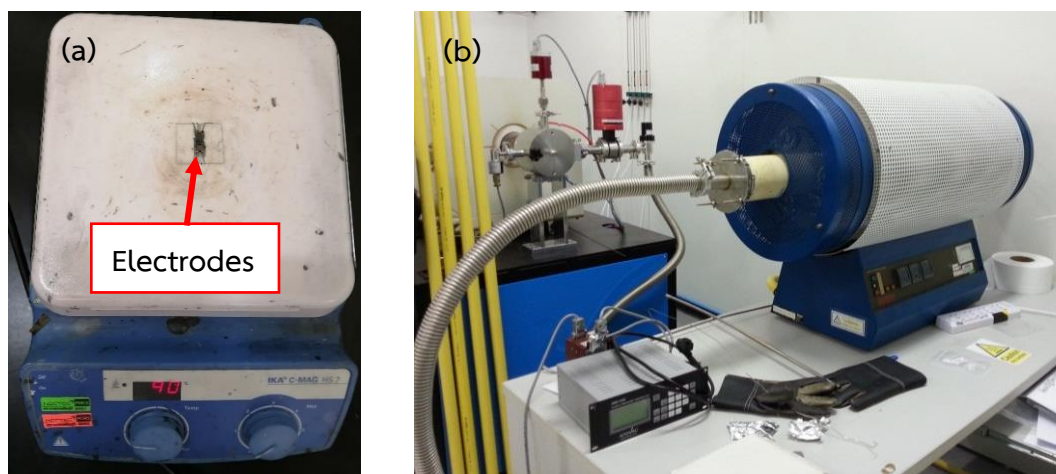
Figure 17 (a) Heating the electrodes on a hot plate (90 °C). (b) A tube furnace used to anneal all the sensors.

4.2 Material characterization

Measuring instrument used in the surface characterization

1. FEG-SEM analysis: TESCAN MIRA3

Scanning electron microscopes (SEM) were used to study morphology. By examining the substrate with a centered electron beam, the Field Emission Gun SEM (FEG-SEM) was used to produce images of the material. The e$^-$ interact with the sample surface's atoms generating different signals that provide detail on the layer morphology and the characteristics of the material.

2. XRD measurements: Shimadzu LabX XRD-6100

X-ray diffraction is employed to describe the crystal structure and the atomic array of materials. It is based on the constructive interference of the monochromatic X-ray and crystalline materials. A Shimadzu LabX XRD-6100 was used to characterized crystal structure and verify phase purity. For one-dimensional nanostructures, the XRD peaks may show the direction of crystal formation.

3. Raman spectroscopy: RENISHAW RE 04

Raman spectroscopy was used to determine vibrational modes of molecules and illustrate the internal structure of molecules and crystals. Raman spectroscopy is

typically used in chemistry to provide structural fingerprints for the recognition of molecules.

4. UV-vis spectroscopy: PG instruments T92+

Ultraviolet-visible (UV-vis) spectroscopy is generally employed in the characterization of transition metal ion solutions and strongly conjugated compounds. And this characterization can measure band-gap from the absorption spectrum. For photons with energies less than the band gap, the standard semiconductor has poor optical absorption, whereas photons with energies greater than the band gap have high absorption. As a consequence, there's also a surge in absorption near the band gap, which manifests itself in UV-Vis's absorbance spectrum as either an absorption edge.

5. Fourier-transform infrared spectroscopy: Perkin Elmer Frontier FTIR

Fourier-transform infrared spectroscopy (FTIR) is a method for measuring an infrared spectrum. The Fourier-transform infrared spectrometer collects high resolution spectral information across a broad spectral spectrum at the same time. This provides a substantial benefit on the nonlinear spectrograph, which calculates frequency across a small spectrum of wavelengths at a period

4.3 Gas testing measurement
Gas testing measurement setup

The gas-sensing properties of MOS nanoparticles were considered towards H_2, CH_4, N_2O, NH_3, $(CH_3)_2CO$, and C_2H_5OH gases by using the flow through technique. To combine the desired concentration of contaminants contained in simulated air, a constant flow of simulated air of 2 l/min was used as a gas carrier.

Every experiment was performed in a temperature-controlled sealed chamber at 20 °C with a steady humidity level. A controlled dc power supply was employed to heat the external NiCr heater to varying operating temperatures. The operating temperature was varied from 200 °C to 350 °C. The working temperature ranged from 200 to 350 °C. Using a computer-controlled device and a voltage-amperometric methodology with a 5

Volt direct current bias (source-measure unit, Keithley 5850) and current measurement through a picoammeter (6487 Keithley PicoAmmeter), the resistances of different sensors were constantly evaluated. To every gas concentration test, the detector was introduced to a gas mixture for 10 minutes then the air flux was restored for 25 minutes. The detected gas concentration was varied from 30 to 2,000 ppm for C_2H_5OH. The experimental set up for gas testing is shown as the following steps.

      1. Prepared sensor probe with the probe inside the chamber (Fig. 18(a)), with the probe touched at both sides of the electrodes (Fig. 18(b) and Fig. 19).

      2. Close the lid of the chamber and check that the gas flow controller is connected to the chamber.

      3. Open the valve for dry air and the measured gas respectively.

      4. Open Brooks *Smart DDE software* for Microsoft[®] Windows™ program and LabVIEW National Instruments™ program. After that, record the following data, the total voltage difference of the circuit (10V), operating temperature (200, 250, 300, 350 $^{\circ}C$), gas concentration range (30 to 2,000 ppm for Ethanol), gas response time (10 minutes), and the sensor recovery time (25 minutes) into the program and press the start button to start the program. The results of gas adsorption measurements are displayed in the graph showing the relationship between resistance and time (Fig. 20).
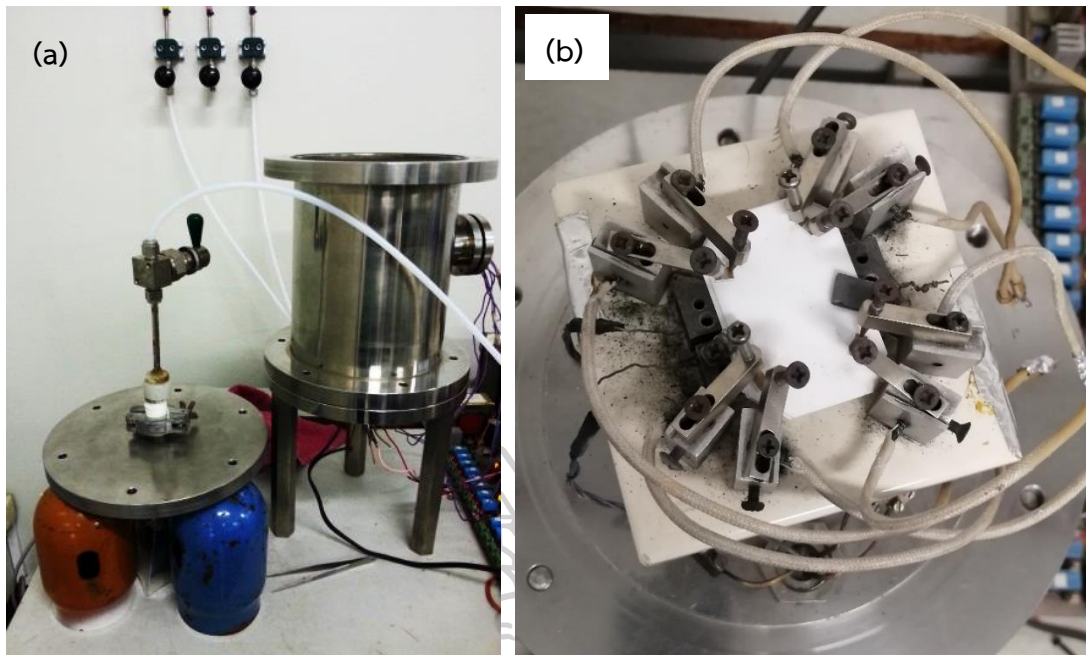
Figure 18 (a) A Chamber used in gas testing system. (b) A probe attached to the electrodes on both sides of the electrodes.
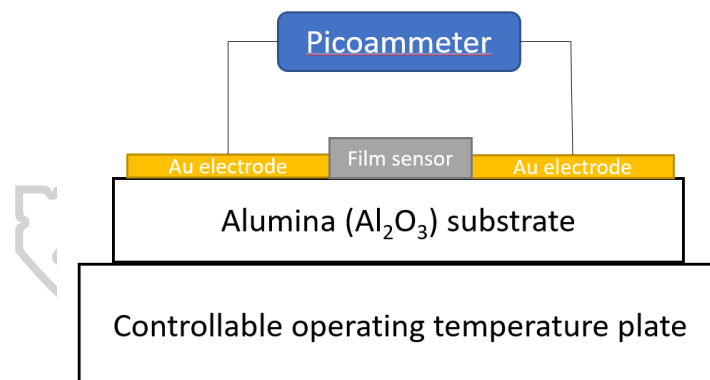
Figure 19 Cross-section of the Sensor.
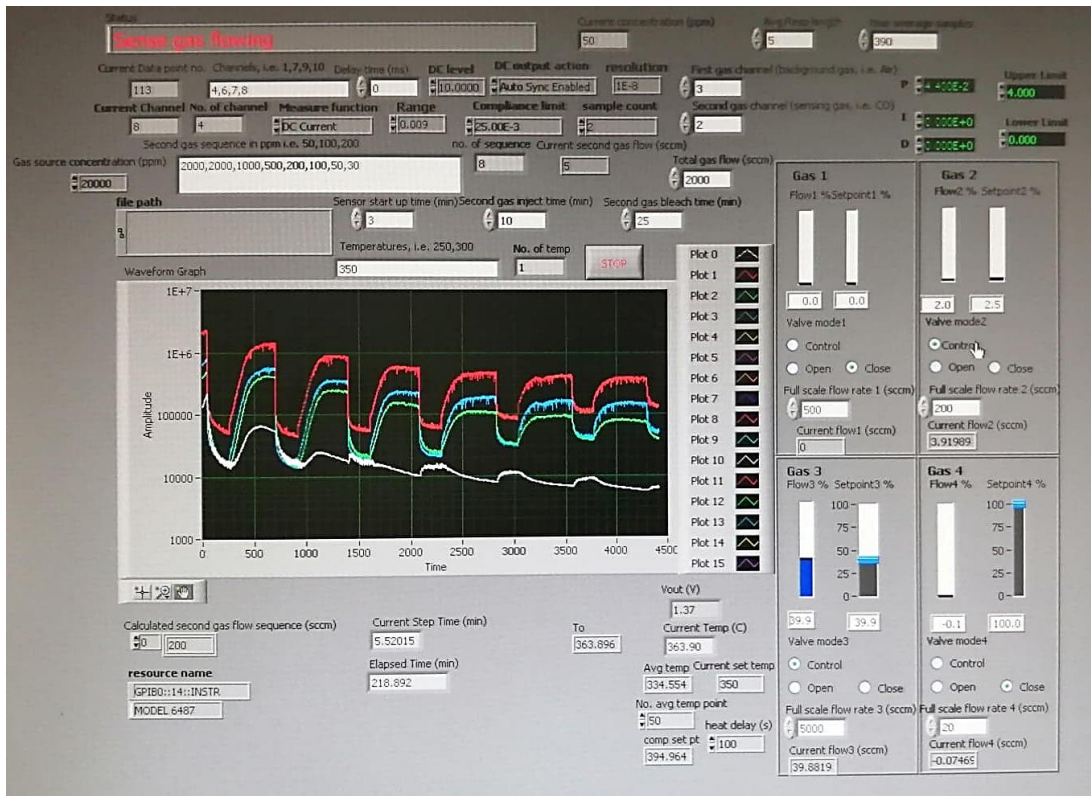
Figure 20 The graph shows the relationship between the resistance value and the time obtained from the gas testing program.
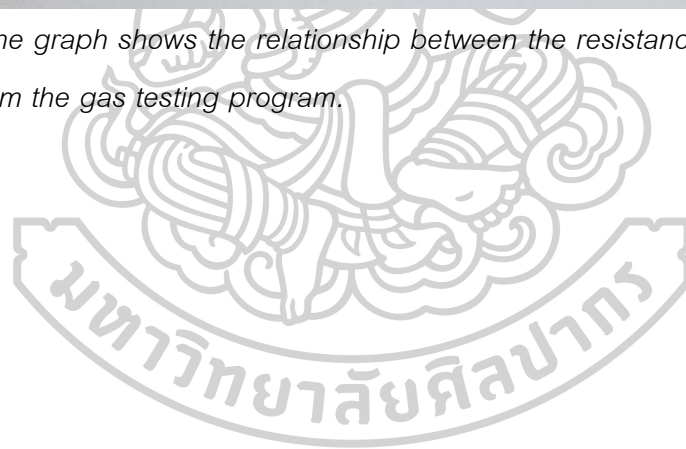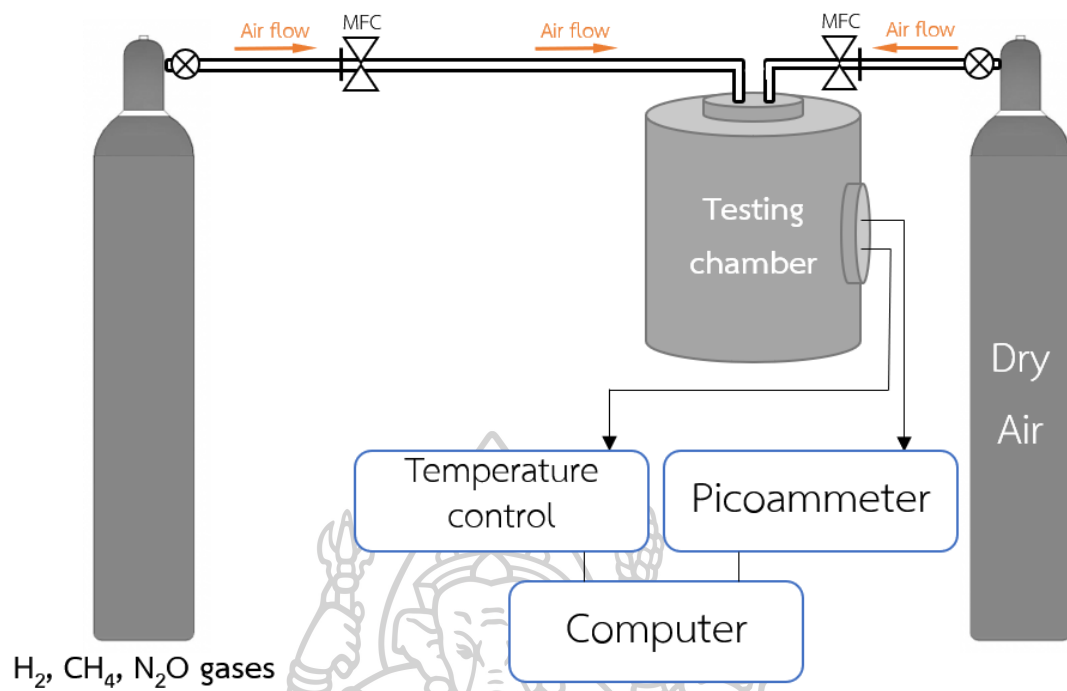
Figure 21 Hydrogen, methane, and nitrous oxide gas measurement system.
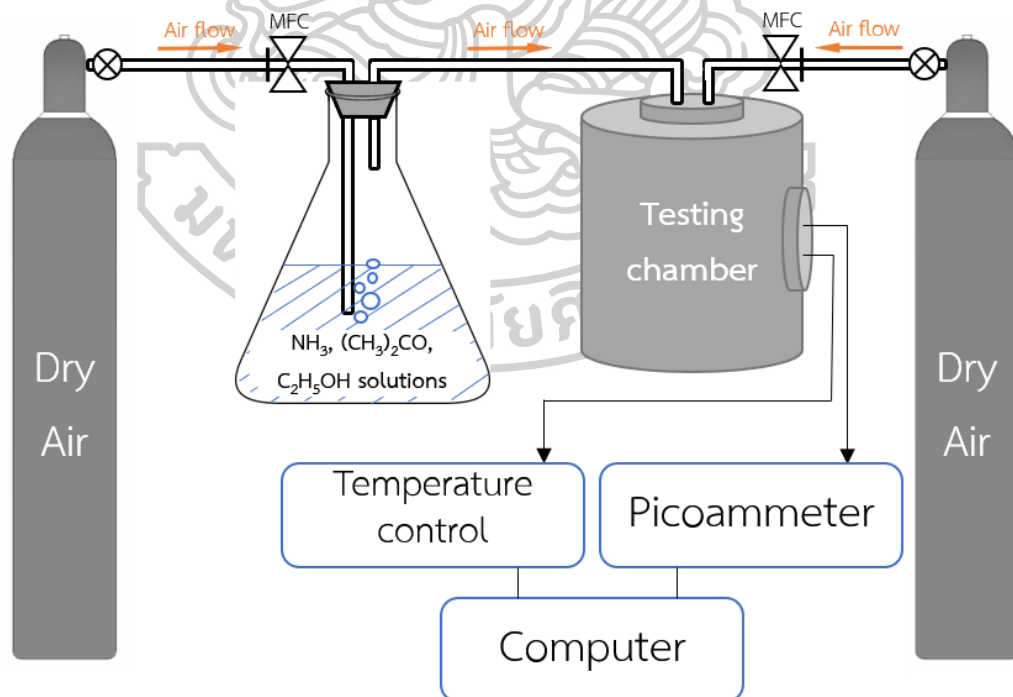
Figure 22 Ammonia, acetone, and ethanol gas measurement system.

Chapter 5

Results and discussion

5.1 Computational study

5.2.1 Design of ZnO/graphene substrates

Pristine ZnO (0001), graphene surface, and ZnO nanocluster ($Zn_{12}O_{12}$)

The first step for calculating all substrates is the optimization of the bulk crystal structure. The initial structure of ZnO was derived from cutting the unit cell containing two O atoms and two Zn atoms along the (0001) direction of bulk wurtzite (Fig. 23). Following that, the atoms and cells were allowed to completely relax and optimize to obtain the double-layer structure of ZnO.
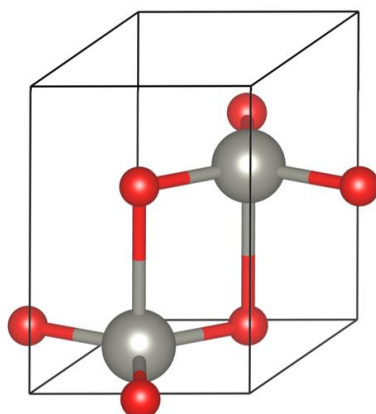
Figure 23 Bulk crystal structure of ZnO.

A single layer 6x6 ZnO unit cell containing 36 Zn atoms and 36 O atoms was cut from the optimized double-layer structure of ZnO. Then it was fully relaxed and optimized, as shown in Fig. 24 (a). The bond length between Zn and O atoms is 1.89 Å (corresponding to [63], which has a bond length of 1.90 Å.), the total energy of the ZnO surface is -312.67 eV. The optimized structure of graphene is shown in Fig. 24(b), with the bond length between C and C of 1.42 Å (corresponding to [64]). Also, ZnO nanocluster ($Zn_{12}O_{12}$) was created, fully relaxed, and optimized (See Fig. 24 (c)). The bond lengths between Zn and O are 1.97 Å, and 1.87 Å (corresponding to [65] which have the bond length of 2.02 Å and 1.85 Å).
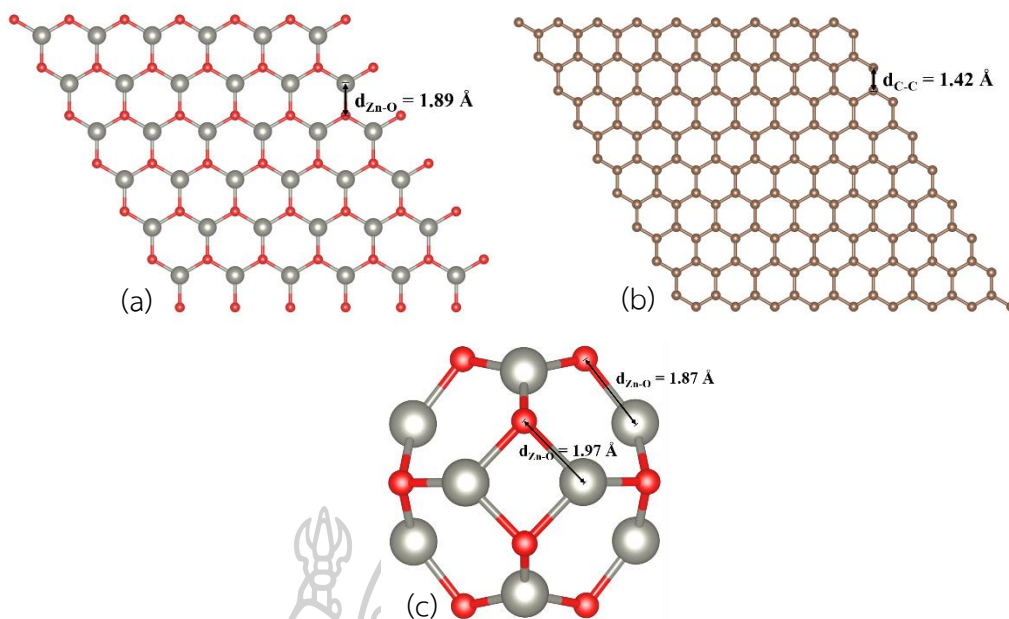
Figure 24 (a) The surface structure of the ZnO plane (0001), (b) The surface structure of the graphene, and (c) The structure of the ZnO nanocluster.

2. ZnO/graphene composite

The addition of graphene to the metal oxide can cause structural properties changes such as changes in inter-molecular bonds or changes in electrical structures that affect the absorption and detection of gas molecules. Therefore, in the present study, the Hybrid ZnO/graphene nanocomposite has been investigated for its gas sensing properties. Accordingly, the three models of hybrid structures are considered as follows:

1. graphene/ZnO, denoted as Gr/ZnO (graphene surface exposed to the gas molecule)

2. ZnO/graphene denoted as ZnO/Gr (ZnO surface exposed to the gas molecule)

3. graphene/$Zn_{12}O_{12}$ denoted as Gr/$Zn_{12}O_{12}$ (ZnO nanocluster surface exposed to the gas molecule)

The composite models, as shown above, were selected to study the effects of the structures and the corresponding electrical and sensing characteristics of the systems upon the gas adsorption.

- Models of graphene/ZnO and ZnO/graphene
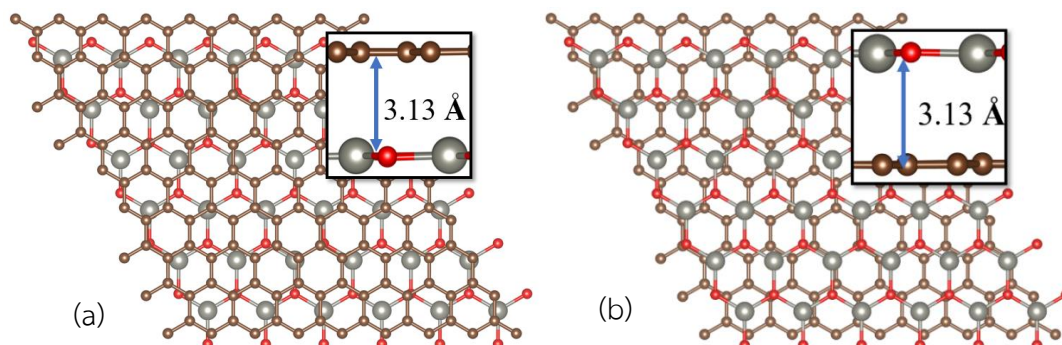
Figure 25 (a) Top view and side view (inset) of the graphene/ZnO and (b) ZnO/graphene structures.

Fig. 25 shows the hybrid structures of graphene/ZnO (a) and ZnO/graphene (b). The distance of the ZnO bond was 1.89 Å, and the interlayer distance between the ZnO and graphene layers was 3.13 Å. These values are in good agreement with the previously reported results [34].

- ZnO nanocluster/graphene

The ZnO nanocluster structure has two different sides, consisting of square and hexagonal faces (See Fig. 24(c)). Based on the two faces, $Zn_{12}O_{12}$ was placed on various sites of the graphene layer to find the most stable structure. The square side of the $Zn_{12}O_{12}$ towards the graphene sheet indicates the adsorption energy of -0.37 eV with the nearest distance between the nanocluster and the graphene of 2.94 Å (Fig. 26). On the other hand, the hexagonal side of the $Zn_{12}O_{12}$ onto the graphene shows the relatively larger E_{ads} = -0.59 eV with the nearest distance between the nanocluster and the graphene of 2.97 Å (Fig. 27).
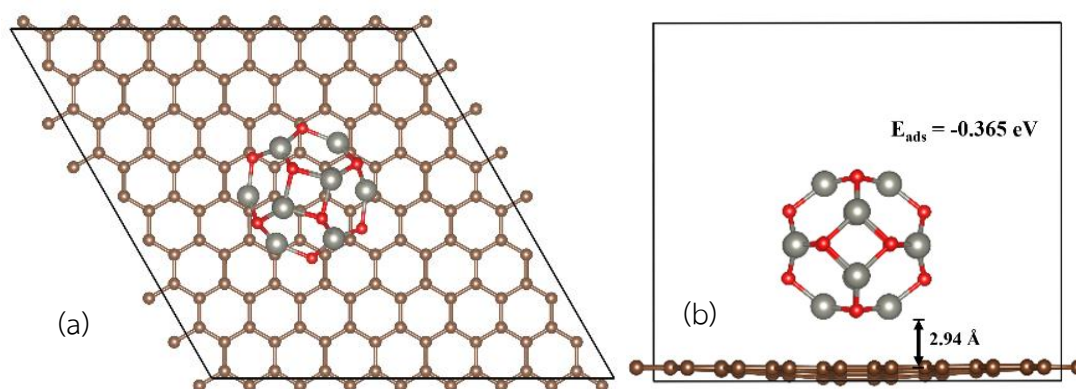
Figure 26 (a) Top view and (b) side view of the structure of graphene/Zn$_{12}$O$_{12}$ (square side).
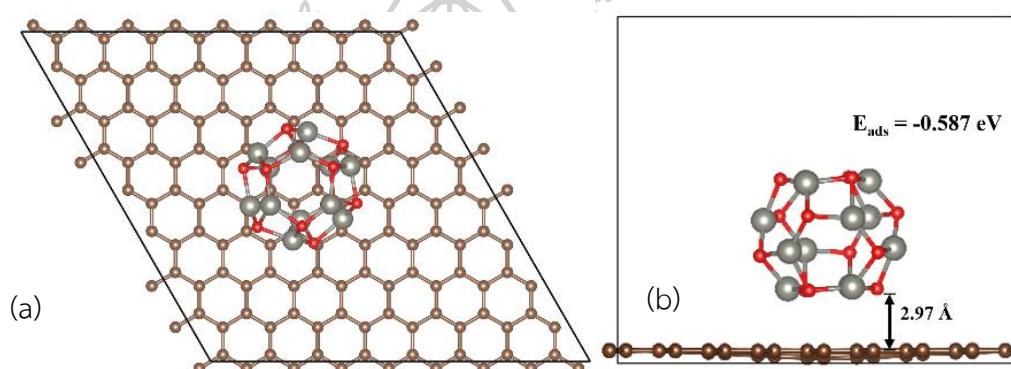
Figure 27 (a) Top view and (b) side view of the structure of graphene/Zn$_{12}$O$_{12}$ (hexagonal side).

5.2.2 Gas adsorption on graphene, ZnO, graphene/ZnO, ZnO/graphene, graphene/Zn$_{12}$O$_{12}$: H$_2$, CH$_4$, and N$_2$O gas molecules

We investigate the adsorption mechanism of H$_2$, CH$_4$, and N$_2$O gas molecules on pristine graphene, ZnO, graphene/ZnO, ZnO/graphene, and graphene/Zn$_{12}$O$_{12}$. We consider all possible adsorption sites of the gas molecule on the substrate with different orientations to find the most preferable configuration. Figure 28 depicts the most preferred binding configurations. It is observable that each gas molecule has different preferences for adsorption sites on the same substrate. Furthermore, CH$_4$ and N$_2$O adsorption has interacted with the ZnO monolayer and slightly distorted the substrate (see Fig. 28(e,f)).

(a) graphene+H_2
E_{ads} = -0.06 eV

(b) graphene+CH_4
E_{ads} = -0.14 eV

(c) graphene+N_2
E_{ads} = -0.16 eV

(d) ZnO+H_2
E_{ads} = -0.08 eV

(e) ZnO+CH_4
E_{ads} = -0.16 eV

(f) ZnO+N_2O
E_{ads} = -0.20 eV

(g) graphene/ZnO+H_2
E_{ads} = -0.07 eV

(h) graphene/ZnO +CH_4
E_{ads} = -0.15 eV

(i) graphene/ZnO +N_2O
E_{ads} = -0.17 eV

(j) ZnO/graphene+H_2
E_{ads} = -0.08 eV

(k) ZnO/graphene+CH_4
E_{ads} = -0.20 eV

(l) ZnO/graphene+N_2
E_{ads} = -0.21 eV

(m) graphene/$Zn_{12}O_{12}$+H_2
E_{ads} = -0.14 eV

(n) graphene/$Zn_{12}O_{12}$+CH_4
E_{ads} = -0.31 eV

(o) graphene/$Zn_{12}O_{12}$+N_2O
E_{ads} = -0.37 eV

Figure 28 The optimized structures and their adsorption energies of graphene (a-c), ZnO (d-f), graphene/ZnO (g-i), ZnO/graphene (j-l), and graphene/$Zn_{12}O_{12}$ (m-o) surfaces after H_2, CH_4, and N_2O adsorption. Top view and side view (insets), where the numbers indicate the distance between the nearest atoms of the substrate and the gas

molecule. The brown, grey, red, silver and white balls represent C, Zn, O, N, and H atoms.

More calculated results of the optimized configurations, such as adsorption energy (E_{ads}), binding distance (d) defined as the distance between the nearest atoms of the substrate and the gas molecule, Fermi energy level (E_F), and charge transfer from the substrate to the gas molecule (ΔQ), are shown in Table 2. The adsorption energies of all structures range from -0.06 eV to -0.37 eV, while the adsorption length range from 2.33 Å to 3.26 Å. All the corresponding adsorption length are relatively large, which indicated that only physisorption exists (E_{ads} < -0.4 eV). Besides that, ΔQ of most complexes is positive, implying the charge is transferred from the substrate to the gas molecule. The absolute values of Eads are summarized in Fig. 29 based on the gas adsorption energy investigation. For all of the gases considered, the graphene/$Zn_{12}O_{12}$ surface could provide the greatest E_{ads} of -0.37 eV for N_2O gas detection. Relatively strong gas adsorption to N_2O is also observed in graphene, ZnO, graphene/ZnO, ZnO/graphene with E_{ads} of -0.16, -0.20, -0.17, and -0.21 eV, respectively, which show the most substantial adsorption to N_2O. More simulated results show that all the substrates poorly interact with the H_2 gas. Thus, among the considered gas species, the hybrid nanocomposite-based gas sensors are the most responsive to N_2O. Among the studied hybrid nanostructures, the graphene/$Zn_{12}O_{12}$ could exhibit the largest E_{ads} of -0.14, -0.31 eV for H_2 and CH_4 gas detection, respectively, meaning that it could be used as a gas sensing material.

Table 2 The calculated adsorption energies of H_2, CH_4, and N_2O on graphene, ZnO, graphene/ZnO, ZnO/graphene, and graphene/$Zn_{12}O_{12}$ surfaces (E_{ads}), adsorption length (d) defined as the length of the nearest atoms of the substrate and the gas molecule, Fermi energy level (E_F), and the charge transfer (ΔQ). The positive value of ΔQ indicates a charge transfer from the substrate to the gas molecule.

Configuration	Gas	E_{ads} (eV)	d (Å)	E_F (eV)	ΔQ (charge transfer)
graphene	H_2	-0.06	2.97	-1.73	-0.4533
	CH_4	-0.14	2.92	-2.20	0.0020
	N_2O	-0.16	3.23	-2.18	0.0142
ZnO	H_2	-0.08	2.49	-3.71	0.0139
	CH_4	-0.16	2.74	-3.68	0.0082
	N_2O	-0.20	3.02	-3.66	0.0231
graphene/ZnO	H_2	-0.07	2.95	-0.90	-0.5070
	CH_4	-0.15	3.09	-1.36	-0.0004
	N_2O	-0.17	3.26	-1.35	0.0122
ZnO/graphene	H_2	-0.08	2.60	-0.72	-0.5454
	CH_4	-0.20	2.66	-1.36	0.0143
	N_2O	-0.21	3.05	-1.34	0.0218
graphene/$Zn_{12}O_{12}$	H_2	-0.14	2.57	-2.88	-0.0046
	CH_4	-0.31	2.61	-2.87	0.0068
	N_2O	-0.37	2.33	-2.86	-0.0025
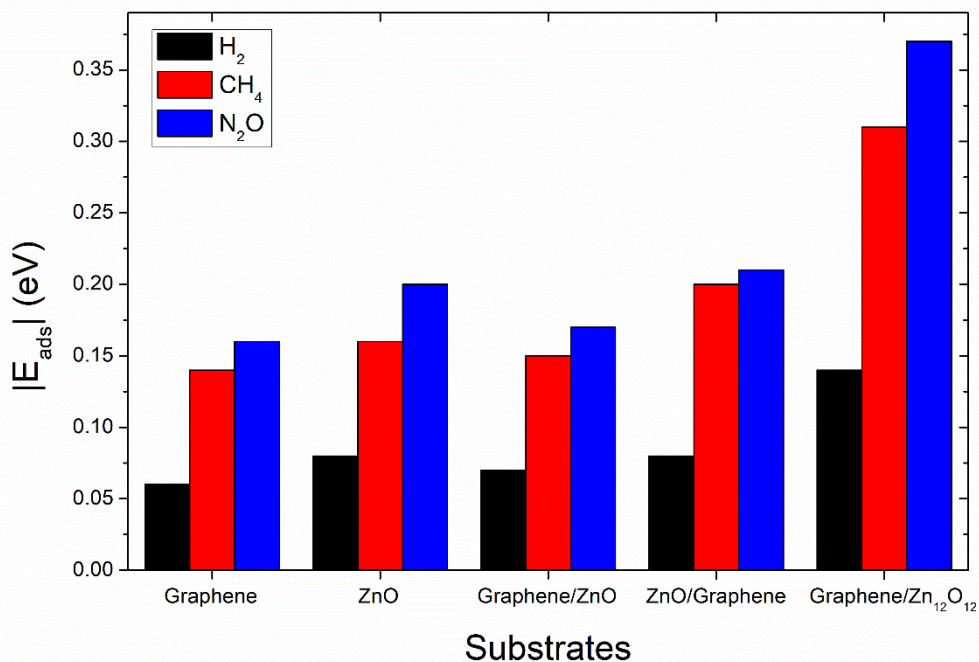
Figure 29 The absolute values of gas adsorption energies ($|E_{ads}|$) of H_2, CH_4, and N_2O on graphene, ZnO, graphene/ZnO, ZnO/graphene, and graphene/$Zn_{12}O_{12}$ substrates.

5.2.3 Electronic structure: DOS, charge transfer

The total density of states (DOS) and the partial density of states (PDOS) were calculated to explore the effects of adsorbed gas molecules on the substrates to their corresponding electronic properties, as shown in Fig. 30. Because of the relatively high charge transfer from H_2 gas molecule to graphene, graphene/ZnO, and ZnO/graphene surface as reported in Table 2 (ΔQ = -0.4533, -0.5070, -0.5454, respectively). Likewise, DOS of H_2 adsorbed on those surfaces has an explicit peak around the Fermi level (see Fig. 30(a), Fig. 31(a, e)). After H_2 adsorbed on graphene, all levels are slightly shifted towards lower energies. Likewise, the DOS of H_2 adsorbed on graphene/ZnO and graphene/$Zn_{12}O_{12}$ have shifted downward, implying that H_2 behaves as an electron donor (charge transfer from H_2 gas molecule to the substrate). For adsorption of other gases, the PDOS (Fig. 30(c)) results reveal peaks around -5 eV in the valence band for CH_4 adsorption and around -4 eV and 2.5 eV (Fig. 30(d)) in the valence and conduction bands for N_2O adsorption, respectively.
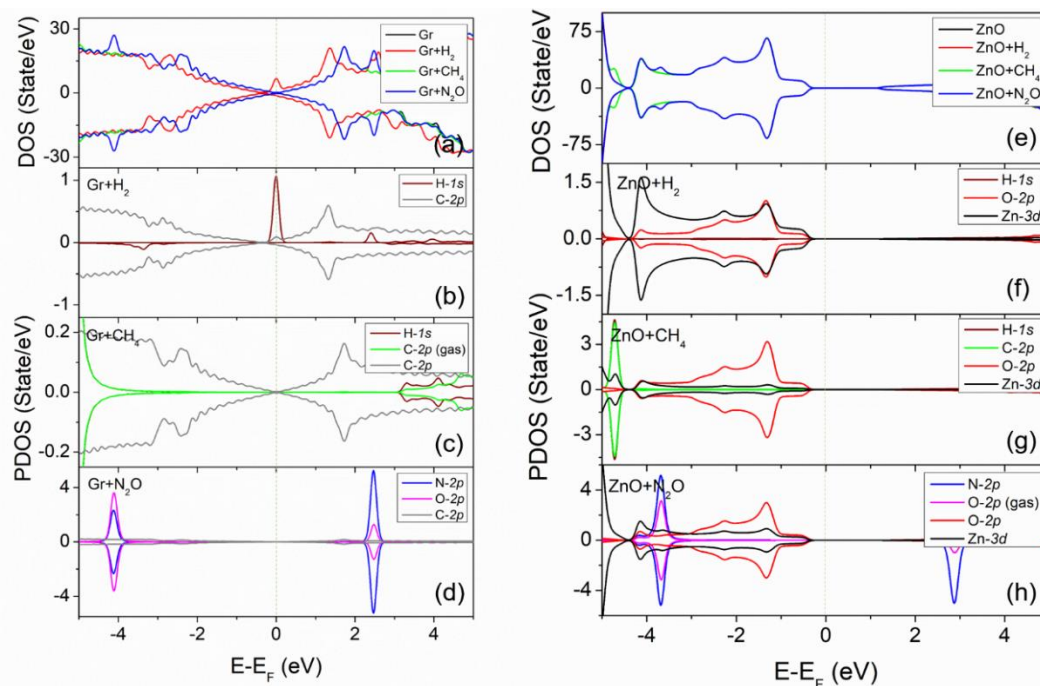
Figure 30 Calculated spin-up and spin-down DOS of (a) graphene and (e) ZnO surface, and the PDOS of graphene (b-d) and ZnO (f-h) surfaces after H_2, CH_4, N_2O gas adsorption.
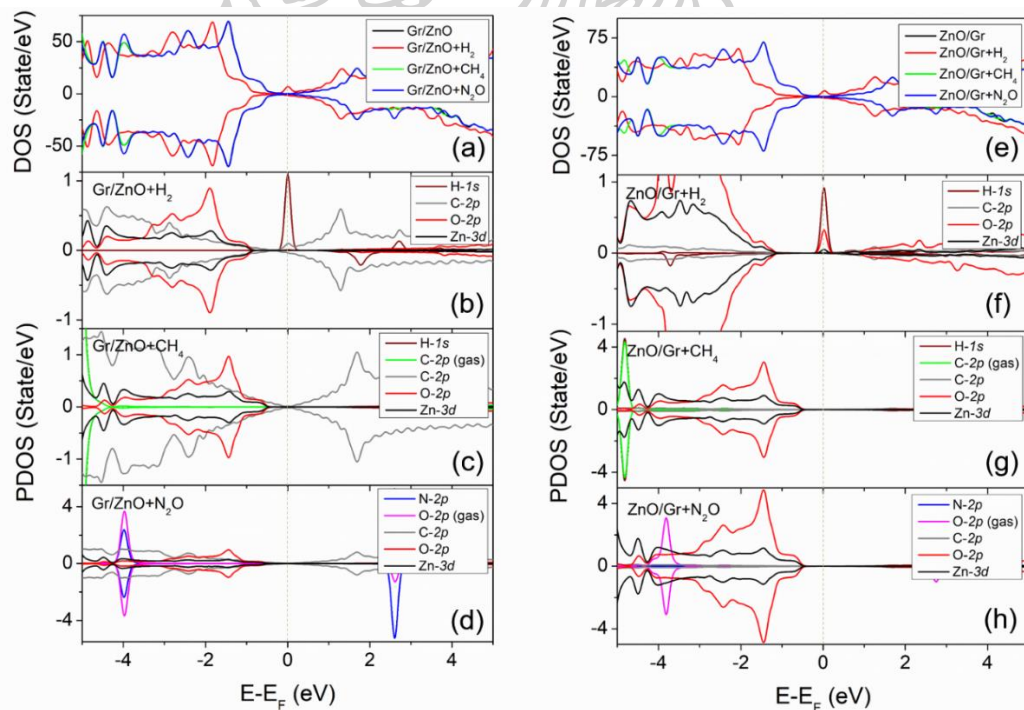
Figure 31 Calculated spin-up and spin-down DOS of (a) graphene/ZnO and (e) ZnO/graphene surface, and the PDOS of graphene/ZnO (b-d) and ZnO/graphene (f-h) surfaces after H_2, CH_4, N_2O gas adsorption.
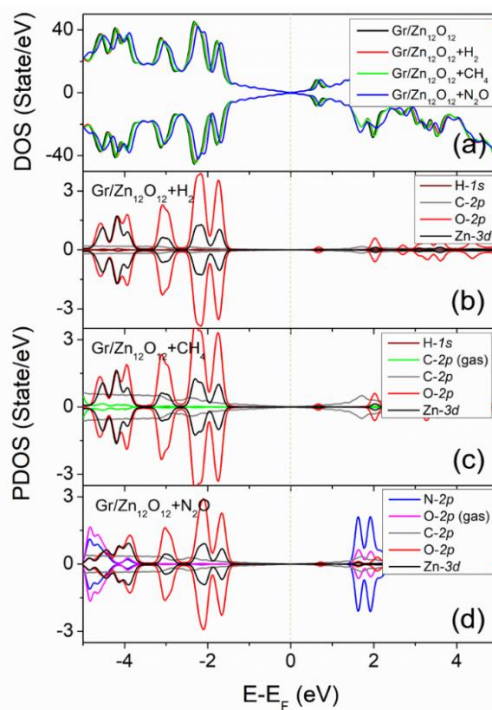
Figure 32 Calculated spin-up and spin-down DOS (a) the PDOS (b-d) of graphene/$Zn_{12}O_{12}$ surfaces after H_2, CH_4, N_2O gas adsorption.

The corresponding electron density differences of graphene, ZnO, graphene/ZnO, ZnO/graphene, and graphene/$Zn_{12}O_{12}$ exposed to H_2, CH_4, and N_2O gas molecules, were calculated and presented in Fig. 33. When all substrates (except ZnO) are exposed to H_2, electronic charges transfer from the H atoms to the atoms at the surface, acting as electron acceptors and donors, as shown in Fig. 33 (a, g, j, m). The different electron affinities of atoms at the surfaces and H atom (H_2) produce a broad electron distribution above the surface upon H_2 adsorption, which means the charge accumulation occurs around C atoms of graphene. In contrast, the charge depletion exists around H (H_2) atoms. This could indicate that electrons transfer from H_2 gas molecules to neighboring C atoms due to the less electronegativity of H atoms. On the other hand, when graphene, ZnO, ZnO/graphene, and graphene/$Zn_{12}O_{12}$ are exposed to CH_4, electronic charges transfer from the substrates to the gas molecule (Fig. 33 (b, e, k, n)). For N_2O adsorption, the O atom of N_2O gas molecules seems to be an electron donor for all substrates. Notably, Fig. 33(m, n, o), we can notice that H_2, CH_4, and N_2O

gas molecules interact with both $Zn_{12}O_{12}$ and graphene layers. Due to the most considerable adsorption energy and their charge transfer capability, it can be expected that graphene/$Zn_{12}O_{12}$ could be a promising gas sensing material for H_2, CH_4, and N_2O gas detection.

(a) graphene+H_2 (b) graphene+CH_4 (c) graphene+N_2O

(d) ZnO+H_2 (e) ZnO+CH_4 (f) ZnO+N_2O

(g) graphene/ZnO+H_2 (h) graphene/ZnO +CH_4 (i) graphene/ZnO +N_2O

(j) ZnO/graphene+H_2 (k) ZnO/graphene+CH_4 (l) ZnO/graphene+N_2O

(m) graphene/$Zn_{12}O_{12}$+H_2 (n) graphene/$Zn_{12}O_{12}$+CH_4 (o) graphene/$Zn_{12}O_{12}$+N_2O
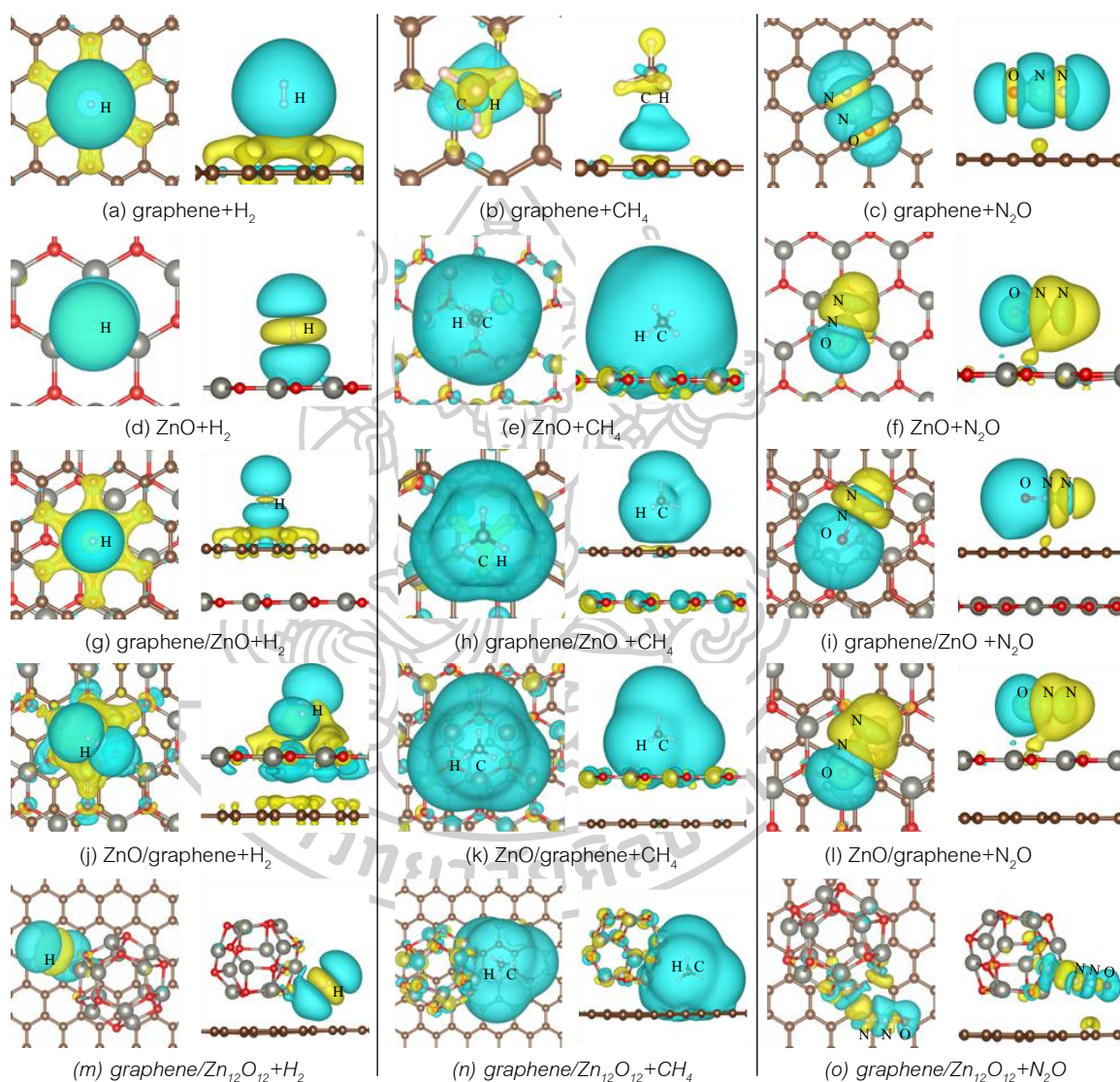
Figure 33 Plots of electron density differences of graphene (a-c), ZnO (d-f), graphene/ZnO (g-i), ZnO/graphene (j-l), and graphene/$Zn_{12}O_{12}$ (m-o) surfaces after H_2, CH_4, and N_2O adsorption. Electron enrichment is represented by yellow, while electron loss is represented by cyan. The isosurface is defined as 0.0005 e/a_0^3 for H_2 and N_2O adsorption and 0.0001 e/a_0^3 for CH_4 adsorption, where a_0 denotes the Bohr's radius.

5.2 Experimental study

      5.2.1 Surface characterization

- Field emission scanning electron microscope analysis

- **The study of the size and shape of ZnO nanoparticles using field emission scanning electron microscope**

After preparing the ZnO nanoparticle using the precipitation method, we used different ethylene glycol (EG) volumes to the solvent since ethylene glycol has a hydrogen-bonding network. In ethylene glycol, both intermolecular and intramolecular hydrogen bonding persist. When metal oxide nanoparticles are dispersed in polar liquids, they have hydroxyl groups on their surfaces [66]. Hydroxyl groups on the surface of nanoparticles are likely to form hydrogen bonds with hydroxyl groups involved in intramolecular and intermolecular hydrogen bonding between ethylene glycol molecules. As a consequence, ethylene glycol's hydrogen bonding network is reorganized. As a result, various aggregate size distributions formed. After that, the products were studied for particle size and shape using a field emission scanning electron microscope (FE-SEM).
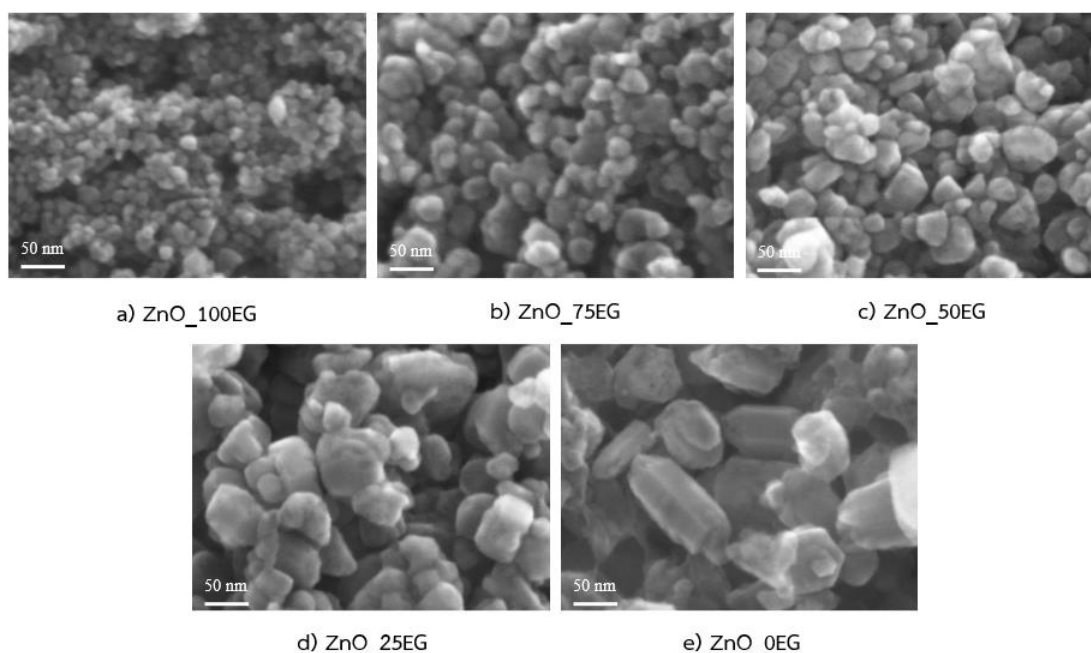
Figure 34 Scanning electron micrographs of ZnO nanoparticles from a 20kv transmitted electron microscope, a magnification of x500k times.

We used 100, 75, 50, 25, and 0 ml of ethylene glycol as a solvent to synthesize ZnO nanoparticles to find the optimum concentration of ethylene glycol, which provides the most diminutive size ZnO nanoparticles. As you can notice from the scanning electron micrograph (Fig. 34(a)), the ZnO particles have a spherical shape and are arranged in order homogeneously with a size of approximately 10 nm. Secondly, (Fig. 34(b)) some particles are larger in size (about 10 to 30 nm). Thirdly, (Fig. 34(c)) most particles have a different shape, and the particle's size is in the range of estimates 10 to 50 nm. In Fig. 34(d), the particles are larger, about 20-60 nm in size. In Fig. 34(e), some particles formed nanorods with an average of 50 nm. And some particles have sizes in a range of 20 to 60 nm, which have various shapes. After all, the five different ZnO nanopowder were examined; we conclude that using 100 ml of ethylene glycol as a solvent (ZnO_100EG) provided the smallest and homogeneous ZnO nanoparticles. Due to the large surface area, it can assume that ZnO_100EG will be a promising sensing material and will be further explored.

- Morphological study of graphene using field emission scanning electron microscope

Graphene was prepared from two high-quality graphite rods through a one-step electrolytic exfoliation method described in Chapter 4. The morphology of single graphene sheets (or stacked multilayer graphene sheets) is similar to waves in a crumple silk veil (Fig. 35). Crumpling and scrolling are inherent characteristics of graphene sheets, as described previously [67]. Under the electron microscope, our graphene sheets appear transparent, suggesting that the properties of electrolytically synthesized graphene are identical to graphene prepared by other methods [68].
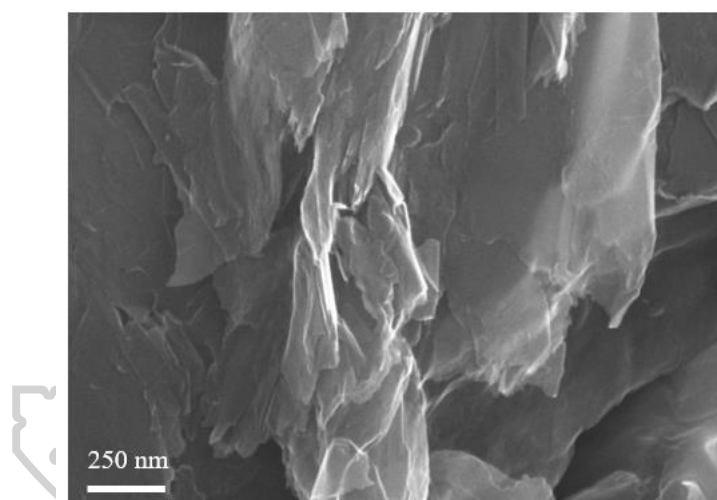
Figure 35 Scanning electron micrographs of graphene from a 20kv transmitted electron microscope, a magnification of x100k times.

- Coexistence characteristics of the graphene-mixed zinc oxide using field emission scanning electron microscope

ZnO nanoparticles were mixed with graphene by physical mixing by varying the graphene amount of 1, 5, and 10 %W/W. After that, the products were studied for particle size and shape by using a field emission scanning electron microscope (FE-SEM). The figure shows an image of pure ZnO (a) and graphene-mixed ZnO (b-d). In Fig. 36(b-d), we observe ZnO nanoparticles are pile together on graphene sheets and

spread among the random stack, crumpled graphene sheets, and closely aligned with one another.

a) Pure ZnO

b) 1% W/W graphene/ZnO

c) 5% W/W graphene/ZnO

d) 10% W/W graphene/ZnO
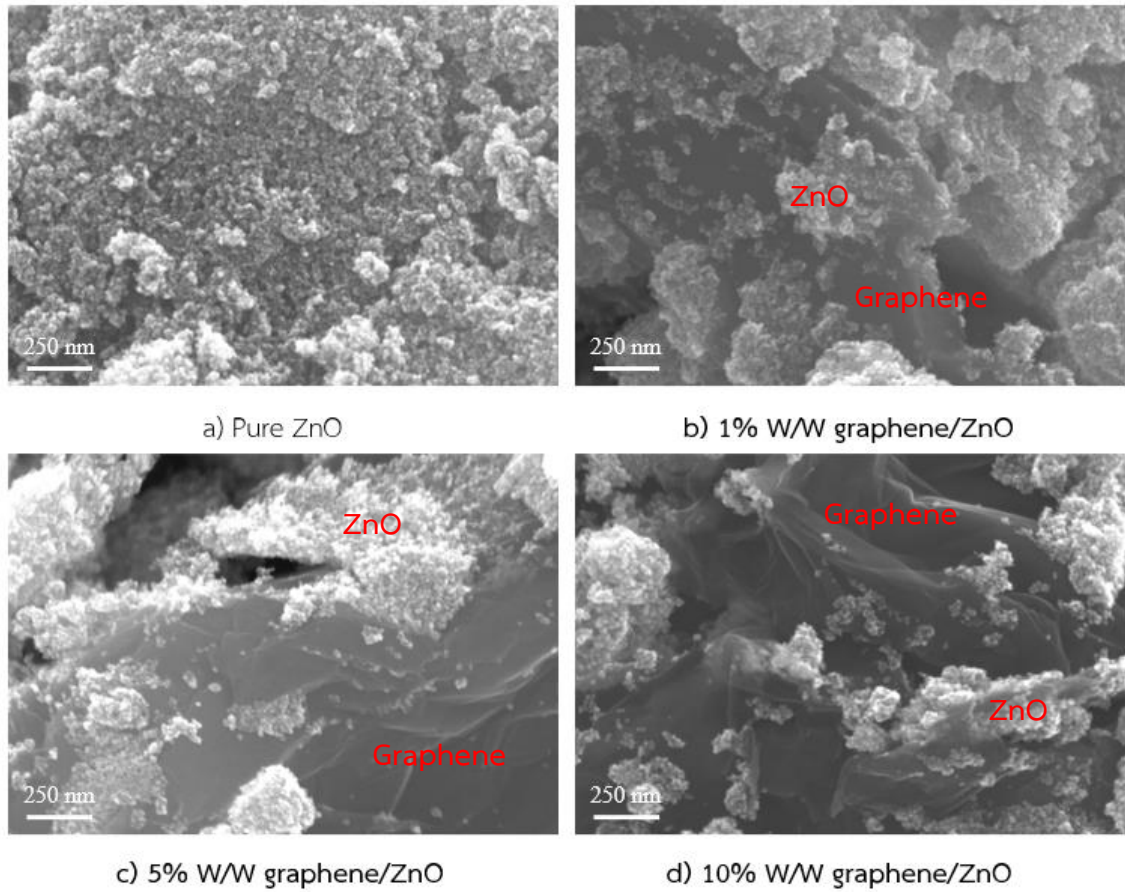
Figure 36 Scanning electron micrographs of pure ZnO and graphene-mixed ZnO from a 20kv transmitted electron microscope, a magnification of x10k times.

- **XRD measurement**

Figure 37 shows the XRD patterns of the synthesized materials. It was found that the ZnO nanoparticles crystallize into a wurtzite hexagonal structure which corresponds to the standard from JCPDS number 89-0510. The dominant peak is (101), (100), and (002). There were also a few minor sharp peaks as well. The diffraction patterns of the nanocomposites do not show any change in comparison with those of pure ZnO. So, the XRD pattern of graphene powder illustrates the characteristics peak of (002) at 26.50° comparable with other works [69].
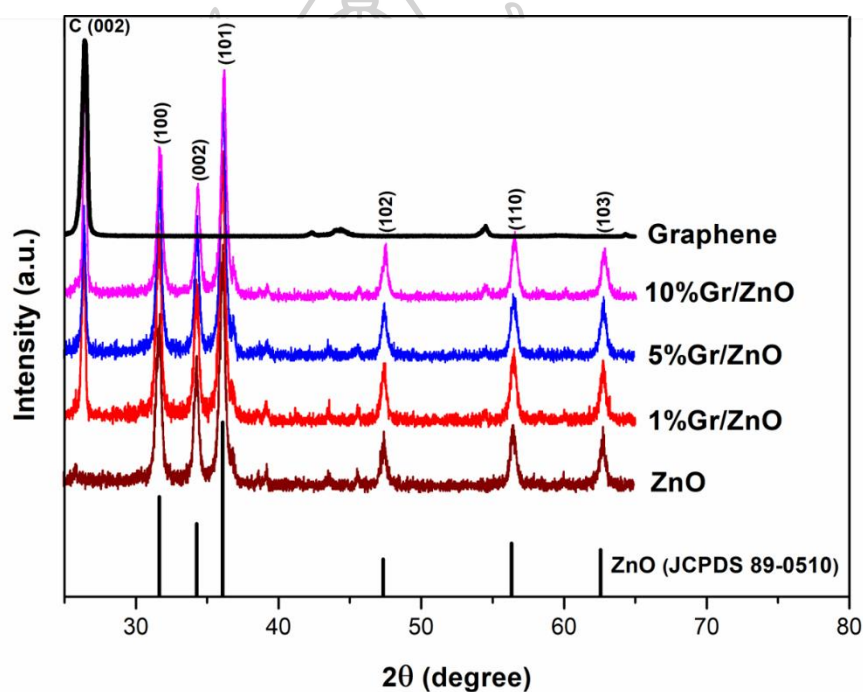
Figure 37 XRD patterns of prepared ZnO and graphene-mixed ZnO with different graphene concentrations.

- Raman spectroscopy

Raman spectroscopy is a non-destructive method for determining defects in graphite materials and the ordered and disordered structures of graphene. The Raman spectrum of the bulk dried graphene powders is demonstrated in Fig. 38. It should be noted that Raman spectra were taken at 3 various spots on each sample, with the median representative spectra being shown. A broad D band (1350 cm^{-1}), sharp G band (1580 cm^{-1}), and 2D band (2658 cm^{-1}) were noticed in the Raman spectrum of the graphene and the graphene/ZnO nanocomposite powders. This specifically demonstrated the existence of graphene in nanocomposites [62]. Due to the defects and partially disordered crystal structure of graphene sheets, chemically synthesized graphene powders usually exhibit a high D band in the Raman spectrum with a strength ratio of $I_D/I_G > 1$ [70]. But this work, the intensity of the G band is slightly higher than that of the D band, meaning that the as-prepared graphene has a low defect content. Multiple-phonon scattering creates peaks located about 1145 cm^{-1} in ZnO samples, but the amplitude of this peak is decreased in graphene/ZnO nanocomposite. Because of the higher scattering and interaction of graphene with ZnO, the Raman peaks corresponding to ZnO in graphene/ZnO nanocomposite are broadened.
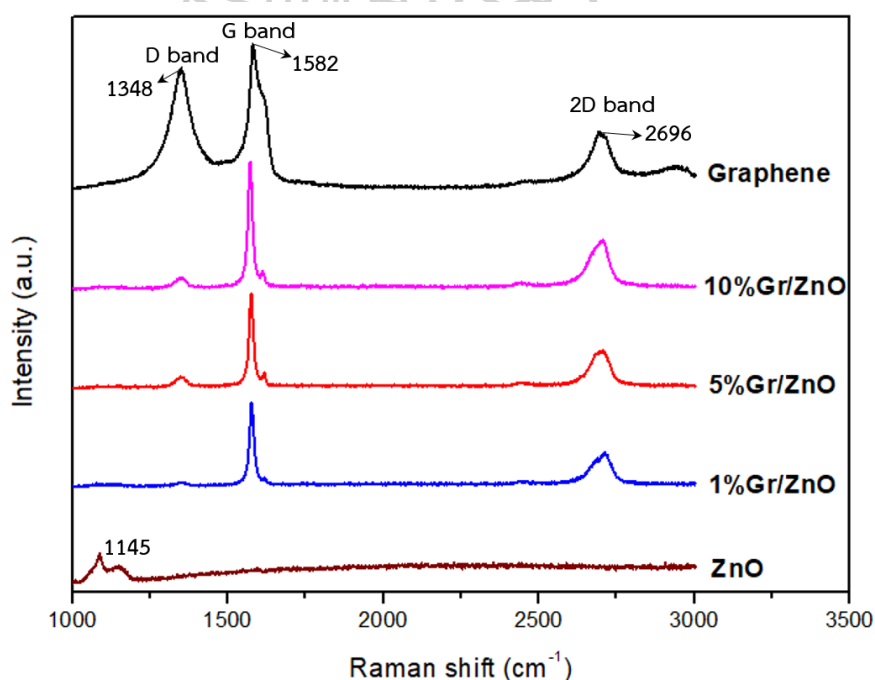
Figure 38 Raman spectra of ZnO, graphene, and graphene/ZnO nanocomposites.

- UV-vis spectroscopy

The optical properties of pure ZnO and graphene/ZnO nanocomposites were investigated by UV-vis absorption spectra. As we know, ZnO is a wide direct bandgap semiconductor, so the [71], $(\alpha h\nu) = K(h\nu - E_g)^{1/2}$, where α is the optical absorption coefficient and $h\nu$ is the energy of an incident photon. E_g is determined by extrapolating the straight-line portion of the curve to $(\alpha h\nu)^2 = 0$. The energy band gaps of pure ZnO and graphene/ZnO nanocomposites are notably different, as seen by the curves of $(\alpha h\nu)^2$ versus $h\nu$ in Fig. 39 for bandgap calculation. ZnO, 1%Gr/ZnO, 5%Gr/ZnO, and 10%Gr/ZnO have bandgap energies of 3.14, 1.73, 1.72, and 1.71 eV, respectively. Hence, graphene has a chemical binding and strong interaction with ZnO cause the considerable bandgap energy changing of the graphene/ZnO nanocomposite.
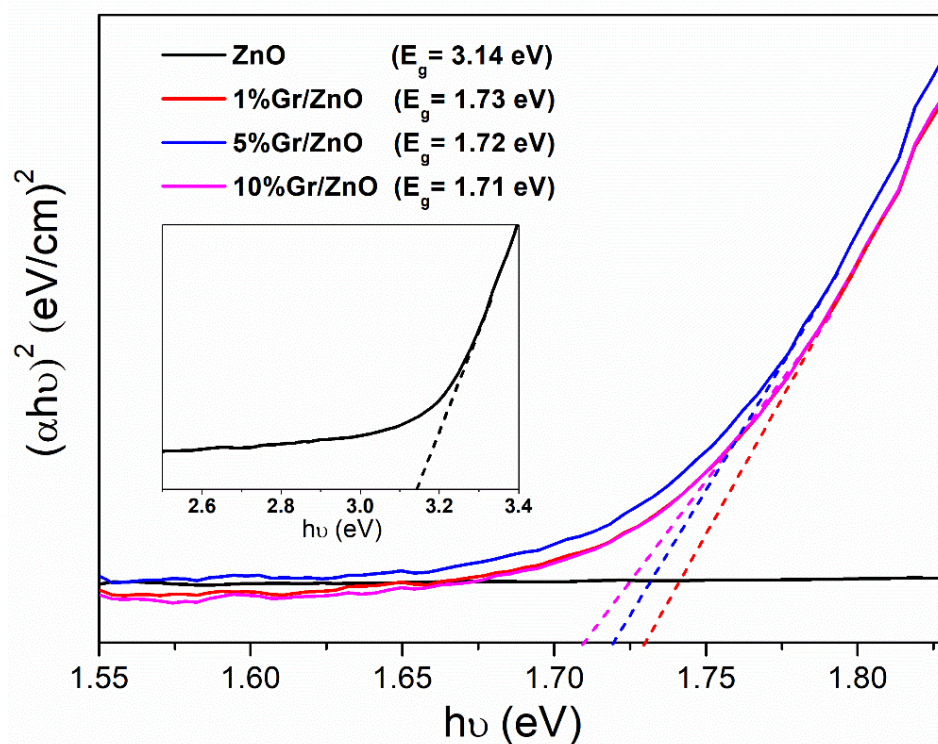
Figure 39 UV-vis absorbance spectra of pure ZnO, and graphene/ZnO nanocomposites.

- **Fourier-transform infrared spectroscopy**

Fourier transforms infrared (FTIR) spectroscopy was employed to identify the functional groups attached to ZnO nanoparticles and graphene, as well as to classify chemical changes in ZnO nanoparticles affected by graphene mixing (Fig. 40). In pure ZnO, the broad absorption located in the range of 3550–3280 cm^{-1} refers to the OH stretching vibration. The peak at 2345 cm^{-1} is due to the symmetric C-H stretching [72]. The peaks at 1433 and 1454 cm^{-1} indicate an OH bending vibration. The small peaks at 843, 758, and 527 cm^{-1} obviously indicate Zn-O stretching [73]. While the graphene/ZnO nanocomposite formation, the peaks at 2087 cm^{-1} are because of Zn-O stretching, suggesting ZnO fastening on the graphene layer, indicating the anchoring of ZnO on the graphene sheet [73].
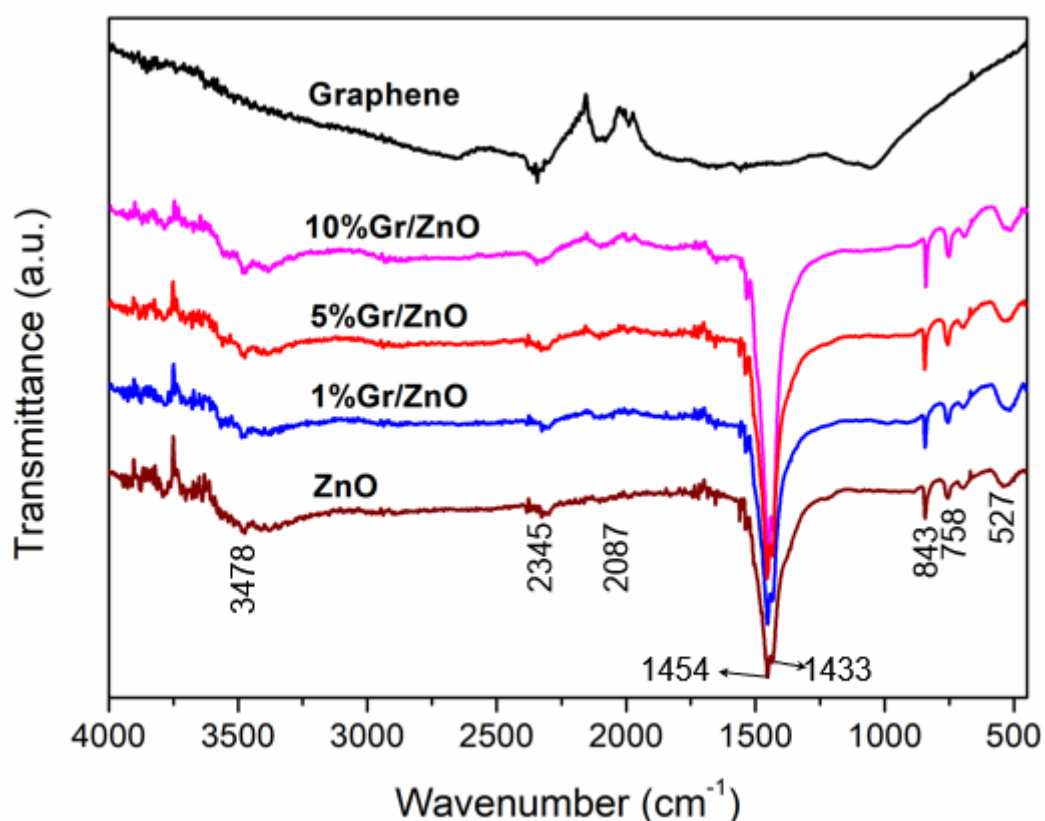
Figure 40 FTIR spectra of ZnO, graphene, and graphene/ZnO nanocomposites.

5.2.2 Gas sensing characteristics

In this experiment, we divided into 2 steps:

   1. Varying temperature to find the optimal temperature for the detected gas, where the highest gas concentration is applied (H_2 30,000 ppm, CH_4 30,000 ppm, N_2O 20 ppm, NH_3 2,000 ppm, $(CH_3)_2CO$ 4,000 ppm, and C_2H_5OH 2,000 ppm). After calculated sensitivity, the further experiment will be performed if it is more significant (S>10).

   2. Varying concentration using the optimal temperature from step 1.

   Fig. 41 shows the correlation between the sensitivity of ZnO and graphene/ZnO nanocomposite sensors towards 30,000 ppm of H_2. The highest H_2-sensing response of 2.87 was achieved by a pure ZnO at an optimum operating temperature of 200 °C, while 1%Gr/ZnO nanocomposite had a lower response (1.91) at its optimum operating temperature of 350 °C.

Figure 41 Sensitivity vs. operating temperature of ZnO and graphene/ZnO nanocomposite sensors toward 30,000 ppm of H_2.

The sensitivity of ZnO and graphene/ZnO nanocomposite sensors toward 30,000 ppm of CH_4 is plotted against operating temperature in Fig. 42. The highest CH_4-sensing response of 3.13 was achieved by a pure ZnO at an optimum operating temperature of 350 °C, while graphene/ZnO nanocomposite had a lower response.

Figure 42 Sensitivity vs. operating temperature of ZnO and graphene/ZnO nanocomposite sensors toward 30,000 ppm of CH_4.

Fig. 43 is the plot for sensitivity vs operating temperature of ZnO and graphene/ZnO nanocomposite sensors toward 20 ppm of N_2O. The highest N_2O-sensing response of 1.22 was achieved by a pure ZnO at an optimum operating temperature of 250 °C, while graphene/ZnO nanocomposite had a lower response.
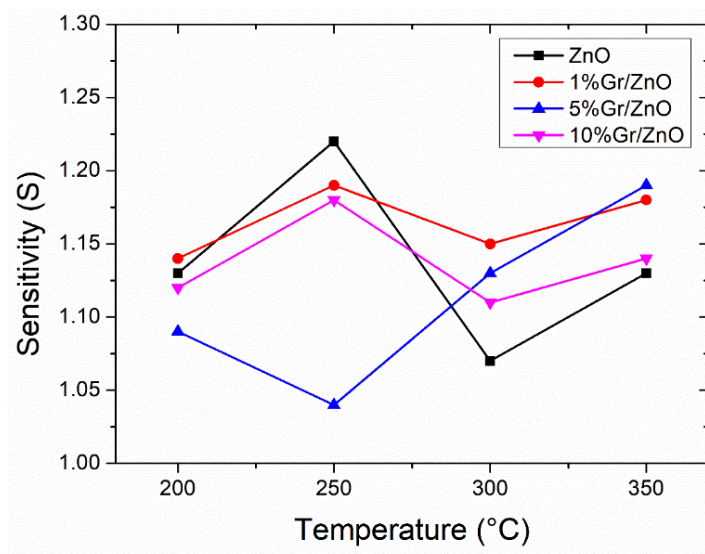
Figure 43 Sensitivity vs. operating temperature of ZnO and graphene/ZnO nanocomposite sensors toward 20 ppm of N$_2$O.

The sensitivity of the nanocomposite sensors towards NH$_3$ at 2,000 ppm concentration at various operating temperatures is shown in Fig. 44. The highest NH$_3$-sensing response of 4.48 was achieved by a 1%Gr/ZnO nanocomposite at an optimum operating temperature of 350 °C. At the same time, pure ZnO had a lower response (3.11) at its optimum operating temperature of 350 °C.
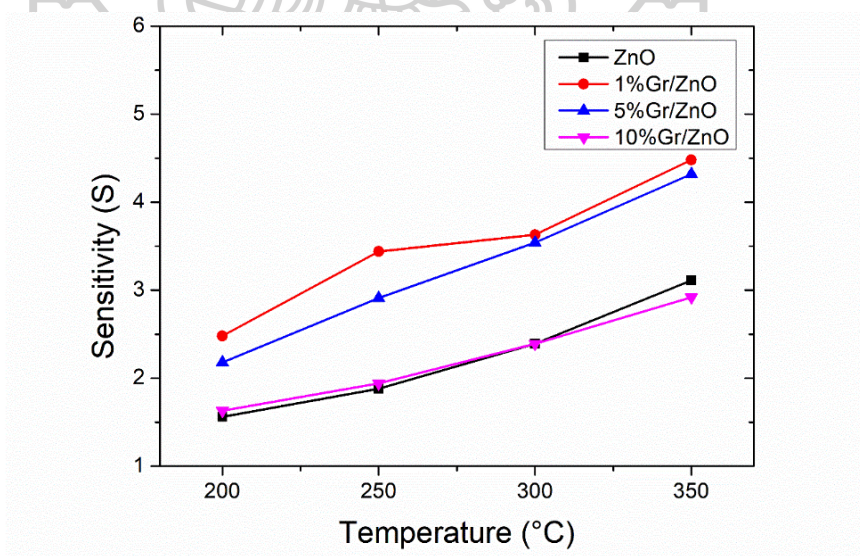
Figure 44 Sensitivity vs. operating temperature of ZnO and graphene/ZnO nanocomposite sensors toward 2,000 ppm of NH$_3$.

Fig. 45 indicates the calculated $(CH_3)_2CO$ sensitivities of pure ZnO and graphene-mixed ZnO films versus operating temperature at 4,000 ppm concentration. At 4 different operating temperatures, the sensitivity of 1,5 and 10 percent graphene-mixed ZnO films towards $(CH_3)_2CO$ was clearly lower than that of pure ZnO. The highest $(CH_3)_2CO$-sensing response of 95.89 was achieved by a pure ZnO film at an optimum operating temperature of 300 °C.
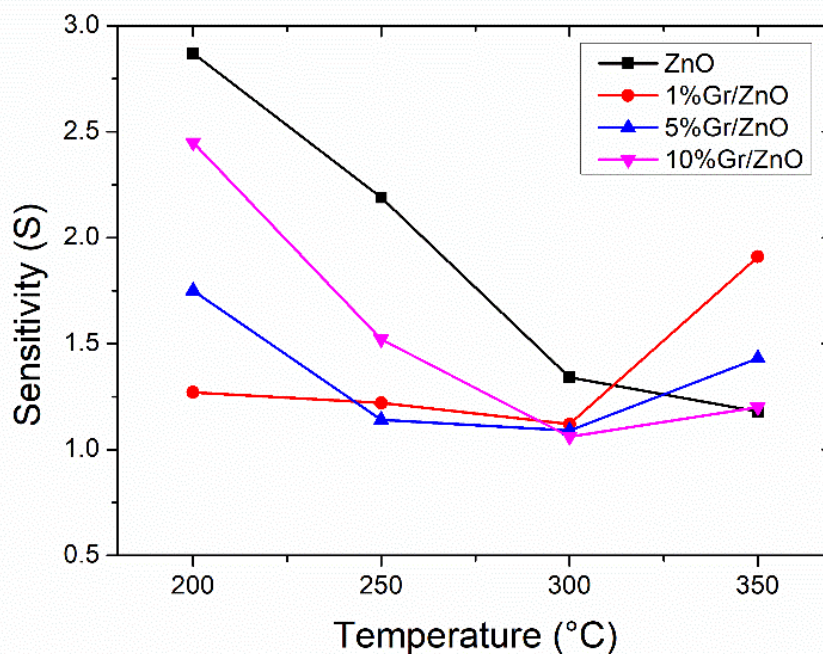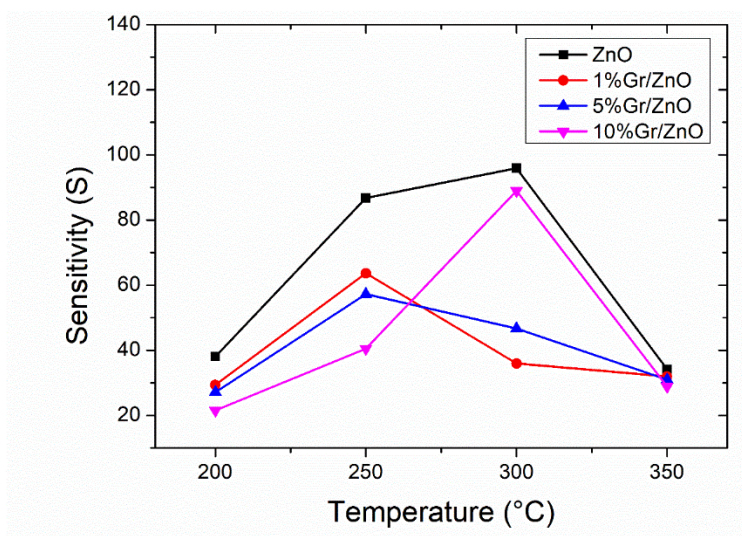

Figure 45 Sensitivity vs. operating temperature of ZnO and graphene/ZnO nanocomposite sensors toward 4,000 ppm of $(CH_3)_2CO$.

The sensitivity of pure ZnO and graphene-mixed ZnO films towards 2,000 ppm C_2H_5OH concentration and operating temperature are shown in Fig. 46. At operating temperatures of 300 and 350 °C, the sensitivities of all graphene-mixed ZnO films to C_2H_5OH were clearly increased when compared to pure ZnO. The highest C_2H_5OH-sensing response of 26.91 was achieved by a 5%Gr/ZnO nanocomposite at an optimum operating temperature of 300 °C, while pure ZnO had a lower response of 12.93 at its optimum operating temperature of 300 °C.
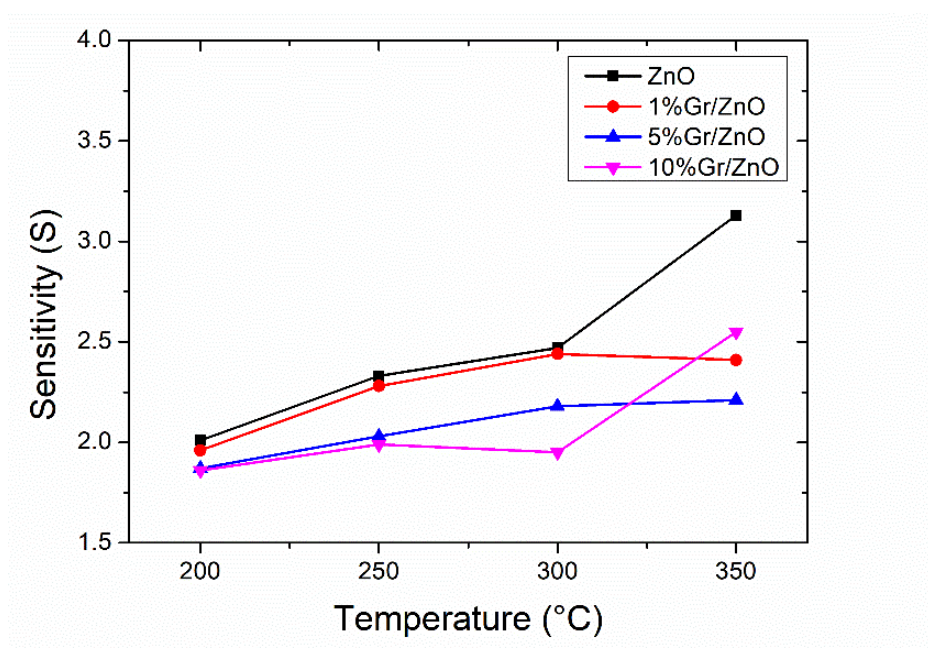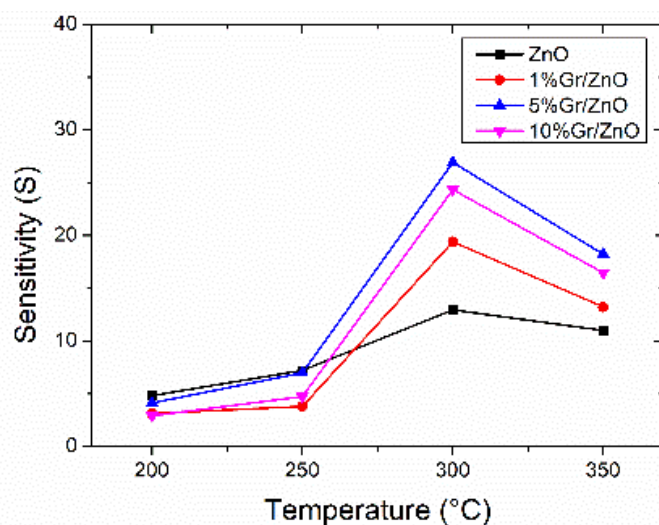
Figure 46 Sensitivity vs. operating temperature of ZnO and graphene/ZnO nanocomposite sensors toward 2,000 ppm of C_2H_5OH.

Following the steps mentioned above, the sensors can respond to C_2H_5OH with a sensitivity of more than 10. So, we continue the experiment to step 2 by varying C_2H_5OH concentration at the optimum temperature of 300 °C (from step 1). Fig. 47 illustrate response plots of the pure ZnO and graphene-mixed ZnO films to C_2H_5OH with the concentration of 30, 50, 100, 200, 500,1,000, and 2,000 ppm at 300 °C. The sensors provide wide concentration ranges for C_2H_5OH detection. Besides that, graphene-mixed ZnO nanocomposite sensors have significantly higher C_2H_5OH responses than bare ZnO nanoparticle sensors. The graphene addition of 5% w/w results in the most significant response when exposed to C_2H_5OH.
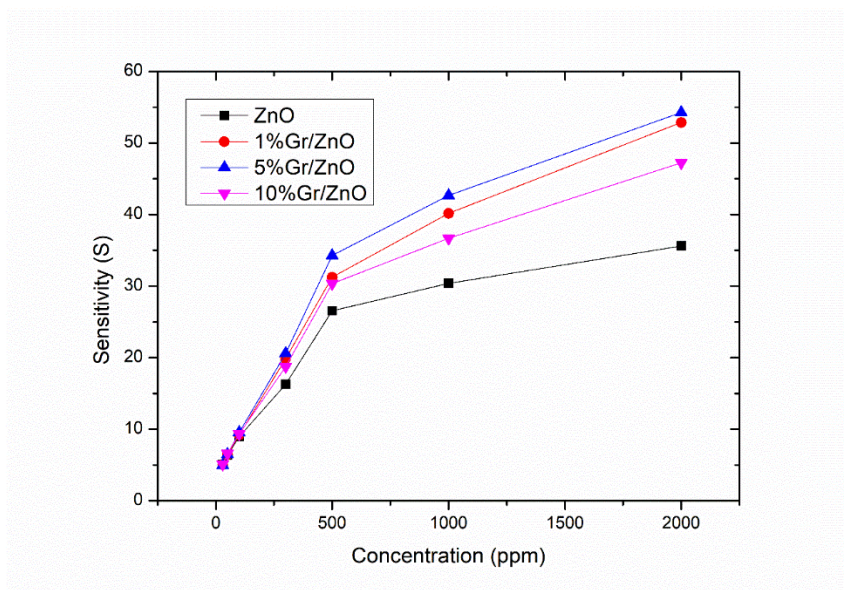
Figure 47 Variation of sensitivity when the gas sensors are exposed to different concentrations of C₂H₅OH at the optimum operating temperature of 300 °C.

The selectivity of the sensors was determined by exposing the sensors based on a 5%Gr/ZnO nanocomposite to 200 ppm C_2H_5OH and other gases, including H_2, CH_4, N_2O, NH_3, and $(CH_3)_2CO$, the selectivity of the sensors was determined. The comparative histogram explicitly reveals that the sensors based on a 5%Gr/ZnO nanocomposite have a significantly higher selectivity to C_2H_5OH vapor as shown in Fig. 48.
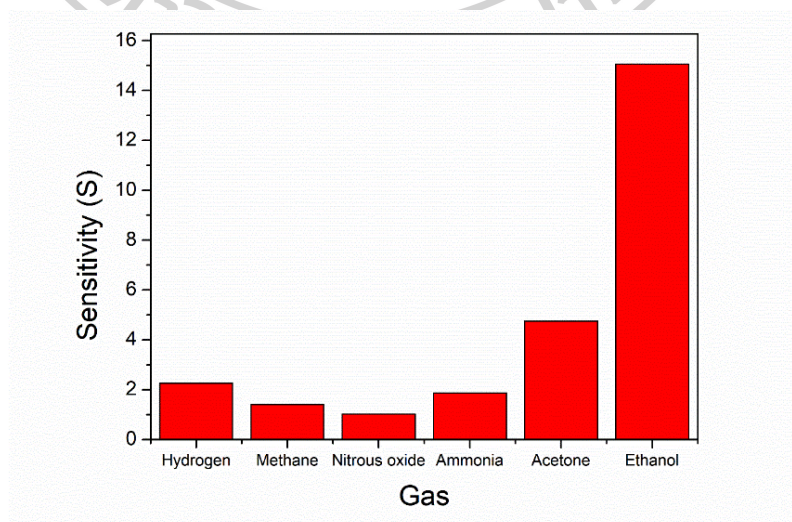
Figure 48 Sensor response of the sensors based on a 5%Gr/ZnO nanocomposite to 200 ppm of different gases at 300 °C.

Table 3 compares the gas sensing efficiency of sensors based on graphene-mixed ZnO nanocomposite and previously mentioned ZnO-graphene materials to ethanol vapor.

Table 3 Comparison of our sensor's sensing capabilities with those of other ethanol sensors that have been reported.

Sensing materials	Method	Gas concentration (ppm)	Operating temperature	Sensitivity	Reference
ZnO/graphene	microwave irradiation	10	300	2.65	[74]
Functionalized graphene/ZnO	modified in situ	200	340	0.95	[75]
graphene/ZnO	in situ	200	150	1.2	[25]
ZnO@ZnS hollow dumbbell–graphene	hydrothermal reaction and sulfurization treatment	1000	210	23	[76]
graphene/ZnO	Chemical precipitation	100	350	9.54	This work

In the computational part, the results show that the graphene/ZnO nanocluster (graphene/$Zn_{12}O_{12}$) appears to be the potential candidate for H_2, CH_4, N_2O gas detection. Using the chemical precipitation method, we synthesized ZnO nanoparticles and selected the smallest size of ZnO nanoparticles. Then the nanoparticles were mixed with graphene resulting in the structure similar to the model proposed by DFT calculations. After that, gas sensors were fabricated from the pure ZnO and graphene-mixed ZnO nanoparticles with 1%, 5%, and 10% of graphene concentration. The gas

sensing results show that the 5% graphene/ZnO at the optimum operating temperature of 300 °C provided the highest sensitivity toward the C_2H_5OH.

The enhanced sensing efficiency of graphene-based composites can be attributed to their increased conductivity. In addition, graphene's large surface area and small structure facilitate the adsorption and diffusion of gas molecules throughout the active surface. Considering the present work, the synthesis technique employed was based on the chemical precipitation, which is a relatively simple and effective. Although the sensitivity of our graphene/ZnO is more significant than in other studies, a higher operating temperature is required. To improve the synergistic effects of graphene and ZnO, further work is needed to optimize the synthesis conditions as well as the gas sensor fabrication.
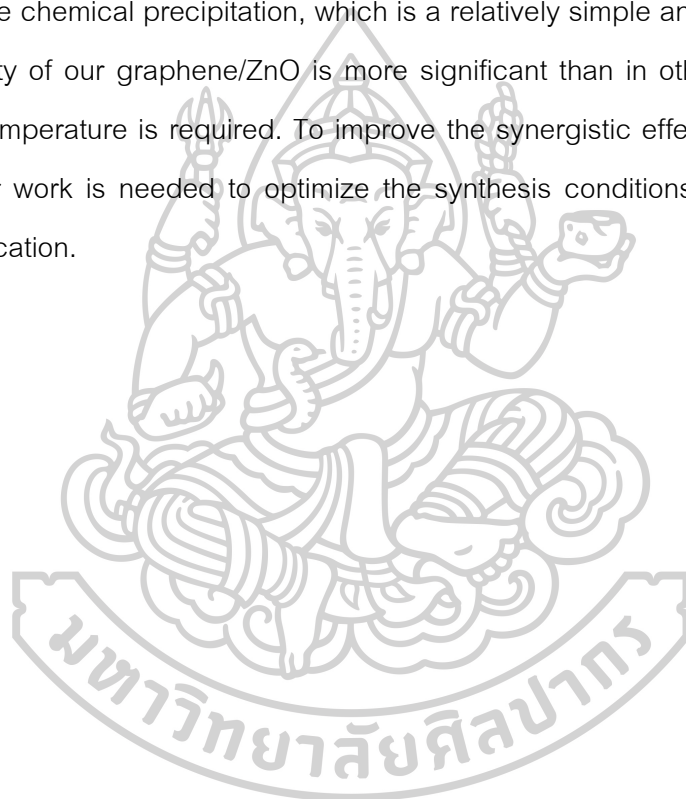
Chapter 6

Thesis Summary and Outlook

In this work, DFT calculations were used to investigate the effect of a graphene-hybrid ZnO layer and the mechanism of enhanced sensing capability. We performed detailed computational analysis on the geometric and electronic transport properties of the 5 different substrates including single-layer graphene, single-layer ZnO (0001), graphene/ZnO, ZnO/graphene, and ZnO nanocluster/graphene upon interaction with different sites of H_2, CH_4, and N_2O gas molecules. According to an analysis of the loading effect, the computed adsorption energy of the gases on the substrates is found to be quite small, in the physisorption range (-0.06 eV to -0.37 eV). The results indicate that the surface modification and the resulting electron transfer mechanism, DOS, and gas adsorption are primarily ascribed for the sensor's gas sensitivity characteristics for H_2, CH_4, and N_2O detection. Moreover, the adsorption energy on ZnO nanocluster/graphene is nearly twice as high as that on pristine and pristine ZnO systems. Our findings indicate that the hybridization of graphene with ZnO can enhances the gas response to H_2, CH_4, and N_2O as compared to pristine ZnO and pristine graphene.

The pure ZnO nanoparticles were successfully synthesized by chemical precipitation method and graphene were prepared from a one-step electrolytic exfoliation method. Then ZnO nanoparticles were mixed with 1, 5, and 10 %W/W of graphene. The sensors were fabricated and tested towards H_2, CH_4, N_2O, NH_3, $(CH_3)_2CO$, and C_2H_5OH with different operating temperatures and gas concentration. The results showed that the appropriate amount of graphene mixing could enhance the C_2H_5OH sensitivity of ZnO sensors. In addition, 5 %W/W graphene-mixed ZnO nanoparticles exhibit the highest sensitivity to C_2H_5OH at all operating temperatures and

concentrations. Especially, this amount of graphene mixing with ZnO sensor illustrates higher C_2H_5OH sensitivity than pure ZnO sensor for 2.5 times. Moreover, the sensitivity of sensor is increased when the ethanol gas concentration is increased with operating temperature of 300 °C

Future Perspective

The study of surface systems and electron transfer will remain to be essential and challenging to research. To continue to design and develop potential devices and reach the stage where practical systems can be easily produced, a lot of experimental and theoretical work is required. In a broader context, density functional theory, as with all computational methods, is constantly being developed and improved, with ongoing efforts to improve accuracy and efficiency. New functionals, scaling behavior, and basis sets, for example, are accurate and allows for faster calculations in a variety of situations. Many other approaches will continue to impart essential work and they will all attempt to answer different questions in this field.

The future of ZnO and graphene in their field of gas detection is undoubtedly broad. ZnO gas sensor have a promising future in industrial and agricultural development, as well as environmental monitoring, due to their sensitivity, selectivity, and small size. Nevertheless, the current large-scale application of ZnO still has difficulties. To enhance its response sensitivity to specific gases, ZnO must be further treated. According to the current development trend, the following aspects may result in increased sensitivity: (1) Increasing specific surface area by modifying the surface and specifically combining it with other nanomaterials; and (2) designing appropriate structure. Enhanced ZnO-based sensitive materials will play an increasingly important role in the future of gas-sensitive materials as research progresses.

REFERENCES

1. Nazemi, H., et al., *Advanced micro-and nano-gas sensor technology: A review.* Sensors, 2019. **19**(6): p. 1285.

2. Yunusa, Z., et al., *Gas sensors: a review.* Sensors and transducers, 2014. **168**(4): p. 61-75.

3. Mahajan, S. and S. Jagtap, *Metal-oxide semiconductors for carbon monoxide (CO) gas sensing: A review.* Applied Materials Today, 2020. **18**: p. 100483.

4. Zhang, J., et al., *Metal-oxide-semiconductor based gas sensors: screening, preparation, and integration.* Physical Chemistry Chemical Physics, 2017. **19**(9): p. 6313-6329.

5. Ji, H., W. Zeng, and Y. Li, *Gas sensing mechanisms of metal oxide semiconductors: a focus review.* Nanoscale, 2019. **11**(47): p. 22664-22684.

6. Wang, C., et al., *Metal oxide gas sensors: sensitivity and influencing factors.* sensors, 2010. **10**(3): p. 2088-2106.

7. Shinde, V., T. Gujar, and C. Lokhande, *LPG sensing properties of ZnO films prepared by spray pyrolysis method: effect of molarity of precursor solution.* Sensors and actuators B: Chemical, 2007. **120**(2): p. 551-559.

8. Gu, H., Z. Wang, and Y. Hu, *Hydrogen gas sensors based on semiconductor oxide nanostructures.* Sensors, 2012. **12**(5): p. 5517-5550.

9. Ghimbeu, C.M., et al., *Electrostatic spray deposited zinc oxide films for gas sensor applications.* Applied Surface Science, 2007. **253**(18): p. 7483-7489.

10. Bakrania, S.D. and M.S. Wooldridge, *The effects of the location of Au additives on combustion-generated SnO2 nanopowders for CO gas sensing.* Sensors, 2010. **10**(7): p. 7002-7017.

11. Zhu, L., W. Zeng, and Y. Li, *A non-oxygen adsorption mechanism for hydrogen detection of nanostructured SnO2 based sensors.* Materials Research Bulletin, 2019. **109**: p. 108-116.

12. Yu, H., et al., *Morphology controllable Fe2O3 nanostructures derived from Fe-*

based metal-organic frameworks for enhanced humidity sensing performances. Sensors and Actuators B: Chemical, 2019. **297**: p. 126744.

13. Dey, K.K., et al., *VO 2 nanorods for efficient performance in thermal fluids and sensors.* Nanoscale, 2015. **7**(14): p. 6159-6172.

14. Gao, X. and T. Zhang, *An overview: Facet-dependent metal oxide semiconductor gas sensors.* Sensors and Actuators B: Chemical, 2018. **277**: p. 604-633.

15. Mitra, P., A.P. Chatterjee, and H.S. Maiti, *ZnO thin film sensor.* Materials Letters, 1998. **35**(1-2): p. 33-38.

16. Feng, X.-c. and Y. Yang. *A new watermarking method based on DWT*. in *International Conference on Computational and Information Science*. 2005. Springer.

17. Sahay, P., et al., *Sprayed ZnO thin films for ethanol sensors.* Journal of materials science, 2005. **40**(18): p. 4791-4793.

18. Wang, J., et al., *Hydrothermally grown oriented ZnO nanorod arrays for gas sensing applications.* Nanotechnology, 2006. **17**(19): p. 4995.

19. Chen, Y.-J., C.-L. Zhu, and G. Xiao, *Ethanol sensing characteristics of ambient temperature sonochemically synthesized ZnO nanotubes.* Sensors and Actuators B: Chemical, 2008. **129**(2): p. 639-642.

20. Dayan, N.J., et al., *A thick-film hydrogen sensor based on a ZnO: MoO3 formulation.* Measurement Science and Technology, 1998. **9**(3): p. 360.

21. Rao, G.T. and D.T. Rao, *Gas sensitivity of ZnO based thick film sensor to NH3 at room temperature.* Sensors and Actuators B: Chemical, 1999. **55**(2-3): p. 166-169.

22. Paraguay-Delgado, F., et al., *Structural analysis and growing mechanisms for long SnO2 nanorods synthesized by spray pyrolysis.* Nanotechnology, 2005. **16**(6): p. 688.

23. Tamaekong, N., et al., *Sensing characteristics of flame-spray-made Pt/ZnO thick films as H2 gas sensor.* Sensors, 2009. **9**(9): p. 6652-6669.

24. Singh, G., et al., *ZnO decorated luminescent graphene as a potential gas sensor at room temperature.* Carbon, 2012. **50**(2): p. 385-394.

25. Anand, K., et al., *Hydrogen sensor based on graphene/ZnO nanocomposite.* Sensors and Actuators B: Chemical, 2014. **195**: p. 409-415.

26. He, J., et al., *Reduced graphene oxide anchored with zinc oxide nanoparticles with enhanced photocatalytic activity and gas sensing properties.* RSC Advances, 2014. **4**(104): p. 60253-60259.

27. Song, N., H. Fan, and H. Tian, *PVP assisted in situ synthesis of functionalized graphene/ZnO (FGZnO) nanohybrids with enhanced gas-sensing property.* Journal of Materials Science, 2015. **50**(5): p. 2229-2238.

28. Kim, H.W., et al., *Synthesis of zinc oxide semiconductors-graphene nanocomposites by microwave irradiation for application to gas sensors.* Sensors and Actuators B: Chemical, 2017. **249**: p. 590-601.

29. Wang, H., et al., *Graphene-like porous ZnO/graphene oxide nanosheets for high-performance acetone vapor detection.* Molecules, 2019. **24**(3): p. 522.

30. Matxain, J.M., et al., *Electronic excitation energies of Zn i O i clusters.* Journal of the American Chemical Society, 2003. **125**(31): p. 9494-9499.

31. Chen, X.-P., et al., *Density-functional calculation of methane adsorption on graphenes.* IEEE Electron Device Letters, 2015. **36**(12): p. 1366-1368.

32. Rao, G., et al., *Adsorption mechanism of graphene-like ZnO monolayer towards CO2 molecules: enhanced CO2 capture.* Nanotechnology, 2015. **27**(1): p. 015502.

33. Meng, R., et al., *Adsorption of Gas Molecules on Graphene‐Like ZnO Nanosheets: The Roles of Gas Concentration, Layer Number, and Heterolayer.* Advanced Materials Interfaces, 2017. **4**(21): p. 1700647.

34. Gholizadeh, R., Y.-X. Yu, and Y. Wang, *N2O adsorption and decomposition over ZnO (0001) doped graphene: Density functional theory calculations.* Applied Surface Science, 2017. **420**: p. 944-953.

35. Pople, J.A., *Nobel lecture: Quantum chemical models.* Reviews of Modern Physics, 1999. **71**(5): p. 1267.

36. Hohenberg, P. and W. Kohn, *Inhomogeneous electron gas.* Physical review, 1964. **136**(3B): p. B864.

37. Kohn, W. and L.J. Sham, *Self-consistent equations including exchange and correlation effects.* Physical review, 1965. **140**(4A): p. A1133.

38. Jones, R.O. and O. Gunnarsson, *The density functional formalism, its applications and prospects.* Reviews of Modern Physics, 1989. **61**(3): p. 689.

39. Ceperley, D.M. and B.J. Alder, *Ground state of the electron gas by a stochastic method.* Physical review letters, 1980. **45**(7): p. 566.

40. Kohn, W., *Nobel Lecture: Electronic structure of matter—wave functions and density functionals.* Reviews of Modern Physics, 1999. **71**(5): p. 1253.

41. Kurth, S., J.P. Perdew, and P. Blaha, *Molecular and solid‐state tests of density functional approximations: LSD, GGAs, and meta‐GGAs.* International journal of quantum chemistry, 1999. **75**(4‐5): p. 889-909.

42. Perdew, J.P., K. Burke, and M. Ernzerhof, *Generalized gradient approximation made simple.* Physical review letters, 1996. **77**(18): p. 3865.

43. Beck, T.L., *Real-space mesh techniques in density-functional theory.* Reviews of Modern Physics, 2000. **72**(4): p. 1041.

44. Monkhorst, H.J. and J.D. Pack, *Special points for Brillouin-zone integrations.* Physical review B, 1976. **13**(12): p. 5188.

45. Blöchl, P.E., O. Jepsen, and O.K. Andersen, *Improved tetrahedron method for Brillouin-zone integrations.* Physical Review B, 1994. **49**(23): p. 16223.

46. Payne, M.C., et al., *Iterative minimization techniques for ab initio total-energy calculations: molecular dynamics and conjugate gradients.* Reviews of modern physics, 1992. **64**(4): p. 1045.

47. Blöchl, P.E., *Projector augmented-wave method.* Physical review B, 1994. **50**(24): p. 17953.

48. Brivio, G. and M. Trioni, *The adiabatic molecule–metal surface interaction: Theoretical approaches.* Reviews of Modern Physics, 1999. **71**(1): p. 231.

49. Groß, A., *Theoretical surface science.* A Microscopic Perspective. Originally published in the series: Advanced Texts in Physics, 2003. **132**.

50. Bach, C. and A. Groß, *Semiclassical treatment of reactions at surfaces with*

electronic transitions. Faraday discussions, 2000. **117**: p. 99-108.

51.   Groß, A., *Reactions at surfaces studied by ab initio dynamics calculations.* Surface science reports, 1998. **32**(8): p. 291-340.

52.   Lischka, M., *Adsorption of simple molecules on structured surfaces*. 2003, Technische Universität München.

53.   Methfessel, M. and A. Paxton, *High-precision sampling for Brillouin-zone integration in metals.* Physical Review B, 1989. **40**(6): p. 3616.

54.   Hammer, B. and M. Scheffler, *Local chemical reactivity of a metal alloy surface.* Physical review letters, 1995. **74**(17): p. 3487.

55.   Eichler, A., J. Hafner, and G. Kresse, *Hydrogen adsorption on the (100) surfaces of rhodium and palladium: the influence of non-local exchange-correlation interactions.* Journal of Physics: Condensed Matter, 1996. **8**(41): p. 7659.

56.   Kresse, G. and J. Hafner, *Ab initio molecular dynamics for liquid metals.* Physical Review B, 1993. **47**(1): p. 558.

57.   Grimme, S., *Semiempirical GGA‐type density functional constructed with a long‐range dispersion correction.* Journal of computational chemistry, 2006. **27**(15): p. 1787-1799.

58.   Henkelman, G., A. Arnaldsson, and H. Jónsson, *A fast and robust algorithm for Bader decomposition of charge density.* Computational Materials Science, 2006. **36**(3): p. 354-360.

59.   Siriwong, C., et al. *Hydrogen and ethanol sensing properties of Pd-loaded ZnO nanoparticles synthesized by flame spray pyrolysis*. in *Advanced Materials Research*. 2016. Trans Tech Publ.

60.   Al-Hardan, N., M. Abdullah, and A.A. Aziz, *The gas response enhancement from ZnO film for H2 gas detection.* Applied Surface Science, 2009. **255**(17): p. 7794-7797.

61.   Chieng, B.W. and Y.Y. Loo, *Synthesis of ZnO nanoparticles by modified polyol method.* Materials Letters, 2012. **73**: p. 78-82.

62.   Karuwan, C., et al., *A disposable screen printed graphene–carbon paste*

electrode and its application in electrochemical sensing. RSC Advances, 2013. **3**(48): p. 25792-25799.

63. Guo, H., et al., *Tunable magnetism in a nonmetal-substituted ZnO monolayer: a first-principles study.* The Journal of Physical Chemistry C, 2012. **116**(20): p. 11336-11342.

64. Xu, P., Q. Tang, and Z. Zhou, *Structural and electronic properties of graphene–ZnO interfaces: dispersion-corrected density functional theory investigations.* Nanotechnology, 2013. **24**(30): p. 305401.

65. Monshi, M.M., S.M. Aghaei, and I. Calizo, *Band gap opening and optical absorption enhancement in graphene using ZnO nanocluster.* Physics Letters A, 2018. **382**(17): p. 1171-1175.

66. Suganthi, K., V.L. Vinodhan, and K. Rajan, *Heat transfer performance and transport properties of ZnO–ethylene glycol and ZnO–ethylene glycol–water nanofluid coolants.* Applied energy, 2014. **135**: p. 548-559.

67. Choi, W., et al., *Synthesis of graphene and its applications: a review.* Critical Reviews in Solid State and Materials Sciences, 2010. **35**(1): p. 52-71.

68. Shams, S.S., R. Zhang, and J. Zhu, *Graphene synthesis: a Review.* Materials Science-Poland, 2015. **33**(3): p. 566-578.

69. Siburian, R., et al., *New route to synthesize of graphene nano sheets.* Oriental Journal of Chemistry, 2018. **34**(1): p. 182.

70. Rezaei, A., B. Kamali, and A.R. Kamali, *Correlation between morphological, structural and electrical properties of graphite and exfoliated graphene nanostructures.* Measurement, 2020. **150**: p. 107087.

71. Avinash, B., et al. *Effect of particle size on band gap and DC electrical conductivity of TiO2 nanomaterial*. in *AIP conference proceedings*. 2016. AIP Publishing LLC.

72. Cao, Y., et al., *Graphene oxide sheets covalently functionalized with block copolymers via click chemistry as reinforcing fillers.* Journal of Materials Chemistry, 2011. **21**(25): p. 9271-9278.

73. Mitra, S., et al., *Efficacy of highly water-dispersed fabricated nano ZnO against clinically isolated bacterial strains.* Applied Nanoscience, 2012. **2**(3): p. 231-238.

74. Van Hieu, N. and N.D. Chien, *Low-temperature growth and ethanol-sensing characteristics of quasi-one-dimensional ZnO nanostructures.* Physica B: Condensed Matter, 2008. **403**(1): p. 50-56.

75. Singh, R.C., et al., *Synthesis of zinc oxide nanorods and nanoparticles by chemical route and their comparative study as ethanol sensors.* Sensors and Actuators B: Chemical, 2008. **135**(1): p. 352-357.

76. Yu, X., et al., *ZnO@ ZnS hollow dumbbells–graphene composites as high-performance photocatalysts and alcohol sensors.* New Journal of Chemistry, 2012. **36**(12): p. 2593-2598.
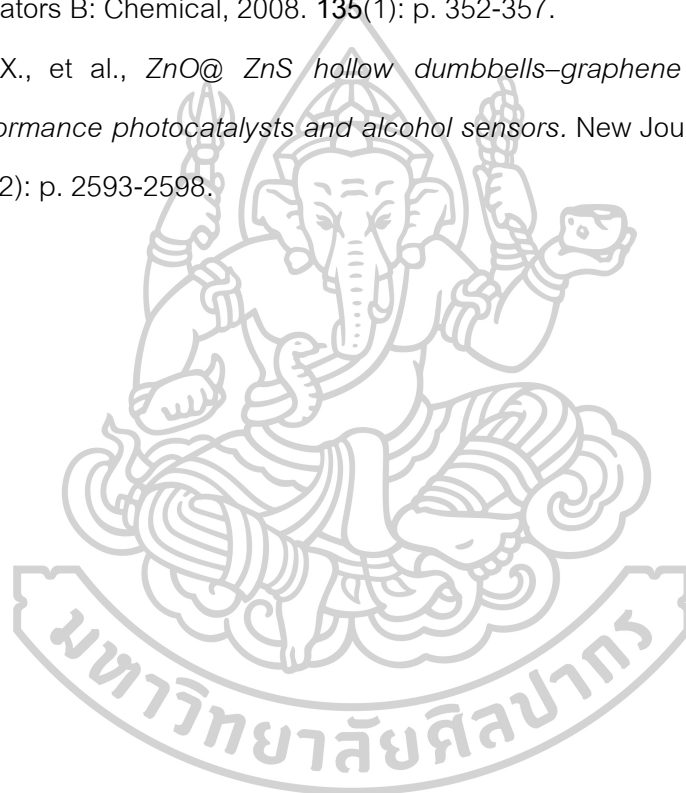
VITA

NAME	Worachote Photaram
DATE OF BIRTH	4 May 1996
PLACE OF BIRTH	Suphanburi
INSTITUTIONS ATTENDED	Bachelor of Science in Physics, Silpakorn University in 2017
HOME ADDRESS	49 Moo 12 Johrakaesamphan, U-Thong, Suphanburi 71170
PUBLICATION	1. Damrongsak, B., Photaram, W., Saengkaew, K., Cheowanish, I., & Damrongsak, P. (2018, July). Apparatus for Inspection of Low-Coercivity Magnetic Force Microscopy Tips. In 2018 International Conference on Engineering, Applied Sciences, and Technology (ICEAST) (pp. 1-4). IEEE.
	2. Photaram, W., Siriwong, C., Aiempanakit, M., Suwanchawalit, C., Liangruksa, M.* (2020). Zinc oxide-graphene nanocomposite for gas sensing applications: A DFT study. The Pure and Applied Chemistry International Conference 2020 (PACCON2020), IMPACT Forum, Muangthong Thani, Nonthaburi, Thailand.